


Emergent strong zero mode through local Floquet engineeringBhaskar Mukherjee¹, Ronald Melendrez,^{2,3} Marcin Szyniszewski¹, Hitesh J. Changlani^{2,3} and Arijeet Pal¹¹*Department of Physics and Astronomy, University College London, Gower Street, London WC1E 6BT, United Kingdom*²*Department of Physics, Florida State University, Tallahassee, Florida 32306, USA*³*National High Magnetic Field Laboratory, Tallahassee, Florida 32304, USA* (Received 10 July 2023; revised 22 December 2023; accepted 2 January 2024; published 8 February 2024)

Periodically driven quantum systems host exotic phenomena that often do not have any analog in undriven systems. Floquet prethermalization and dynamical freezing of certain observables, via the emergence of conservation laws, are realized by controlling the drive frequency. Recent experimental developments in synthetic quantum matter, such as superconducting qubits and cold atoms, have opened avenues for implementing local Floquet engineering which can achieve spatially modulated quantum control of states. Here, we uncover the novel memory effects of local periodic driving in a nonintegrable spin-half staggered Heisenberg chain. For a boundary-driven protocol at the dynamical freezing frequency, we show the formation of an approximate strong zero mode, a prethermal quasilocal operator, due to the emergence of a discrete global \mathbb{Z}_2 symmetry. This is captured by constructing an accurate effective Floquet Hamiltonian using a higher-order partially resummed Floquet-Magnus expansion. The lifetime of the boundary spin can be exponentially enhanced by enlarging the set of suitably chosen driven sites. We demonstrate that in the asymptotic limit, achieved by increasing the number of driven sites, a strong zero mode emerges, where the lifetime of the boundary spin grows exponentially with system size. The nonlocal processes in the Floquet Hamiltonian play a pivotal role in the total freezing of the boundary spin in the thermodynamic limit. The novel dynamics of the boundary spin is accompanied by a rich structure of entanglement in the Floquet eigenstates where specific bipartitions yield an area-law scaling while the entanglement for random bipartitions scales as a volume-law. Our work addresses the long-standing question of the existence of a strong zero mode in a nonintegrable model and elucidates the complex nature of thermalization in locally driven systems.

DOI: [10.1103/PhysRevB.109.064303](https://doi.org/10.1103/PhysRevB.109.064303)**I. INTRODUCTION**

Protection of quantum information in many-body systems in the presence of decoherence is vital for quantum information processing [1–3]. Realizations in physical systems of qubits are routinely subjected to periodic drives using optical and microwave resonators for quantum control [4–6]. Driving systems away from equilibrium is an experimental prescription for lengthening the lifetime of qubits. The potential of periodic driving to produce novel phases of matter characterized by dynamical localization [7,8], topology [9–13], and time crystallinity [14–21] (which often does not have any equilibrium counterpart) has been explored in detail both theoretically and experimentally. Realizing exotic dynamical states through Floquet engineering has witnessed a surge in theoretical interest [22–26] in recent years. In interacting, driven systems thermalization to infinite temperature provides a major roadblock to the protection of entanglement and correlations [27,28]. In the absence of disorder, quantum many-body scars (QMBS) [29–37], Hilbert-space fragmen-

tation [38–43], and disorder-free localization [44,45] have provided instances where local thermalization can be avoided due to constraints in the interaction.

Certain one-dimensional many-body Hamiltonians are endowed with a quasilocal operator called a strong zero mode (SZM), which exists on the boundary of the system and is conserved for long times [46,47]. This operator can be utilized to encode stable quantum information away from the ground state and does not require low temperatures. The existence of SZM can be proven in integrable models while in the presence of weak integrability-breaking perturbations, these quasilocal operators are expected to exhibit prethermal behavior [48–50]. Models with Hilbert space fragmentation can host a statistically localized SZM, without the presence of integrability [51]. The connection between integrability and SZMs is of significant interest for the breakdown of thermalization. In this context, symmetries play a crucial role in fragmenting the Hilbert space and forming quantum scars, which stabilize SZM. This class of phenomena falls under the rubric of partially integrable models, where local dynamical properties exhibit nonthermal behavior. Under a global periodic drive that breaks integrability while preserving the global symmetry, the SZM destabilizes and has a finite lifetime [52,53]. These boundary observables take a parametrically long time to thermalize while the bulk of the system thermalizes quickly. These approximate zero modes are continuously connected to

Published by the American Physical Society under the terms of the Creative Commons Attribution 4.0 International license. Further distribution of this work must maintain attribution to the author(s) and the published article's title, journal citation, and DOI.

exact zero modes in the integrable limit of the models. Indeed, in most cases, the presence of a global drive appears to be crucial for realizing prethermal or athermal behavior due to the emergence of conservation laws.

Generically, an interacting Floquet system heats up to an infinite temperature state, however, prethermal or slow dynamics can be induced due to the separation of scales between the frequency of the drive and the system's internal energy scales [17,54–58]. The distinct stroboscopic dynamical regimes of a periodically driven system are governed by the Floquet Hamiltonian H_F , defined through the propagator $U(\tau)$ as

$$U(\tau) = \mathcal{T} \exp\left(-i \int_0^\tau H(t') dt'\right) = \exp(-iH_F \tau), \quad (1)$$

where $H(t) = H(t + \tau)$. H_F plays a central role in understanding the slow dynamics or heating to infinite temperature [59–61]. A perturbative description of the prethermal timescales can be developed in terms of an expansion of H_F in τ , where τ is the time-period of the Floquet drive. In general, the perturbative corrections in a periodically driven nonintegrable system become nonlocal and the series diverges in the thermodynamic limit, signaling rapid thermalization. However, through appropriate Floquet engineering, one can prolong the prethermal behavior to experimentally observable times enhancing the radius of convergence of such perturbation series. For example, in the presence of a high-frequency drive, nonintegrable systems can exhibit prethermal behavior where emergent conservation laws are applicable for exponentially long times. In another class of phenomena, global drives can result in the formation of Floquet quantum scars [62–67] and dynamical many-body freezing [68–70], where local observables remain athermal under unitary evolution for a specific choice of drive protocols—an exclusively drive-induced nonthermal phenomenon at intermediate frequencies. The frozen states are characterized by local conservation laws and lead to scarring of the Floquet spectrum.

A question naturally emerges, what happens when a system is driven locally? Unlike the global drive which can preserve translational symmetry, a local drive explicitly breaks it. Recently, the real-space profile of thermalization for local or spatially modulated drives has been shown to exhibit rich behavior where the drive can disentangle spins leading to large variations in thermalization times and even steady-state properties [71,72]. The disentangling effect of the drive can generate *cold spots* which persist for significantly longer than thermalization times in the rest of the system.

In this work, we consider the fate of thermalization for a boundary-driven nonintegrable spin chain. In the absence of driving, the model hosts a set of scarred eigenstates that act as a large spin given by the $SU(2)$ symmetry of the model, showing persistent oscillations for certain unentangled initial states. In the presence of a local drive, this manifold is destroyed by a novel form of dynamical disentangling of the spin due to the emergence of a discrete symmetry at the dynamical freezing frequency. We unravel a new mechanism for local ergodicity breaking due to the formation of an approximate SZM at a certain discrete set of frequencies. Furthermore, using Floquet engineering of a cluster of sites (see the illustration in

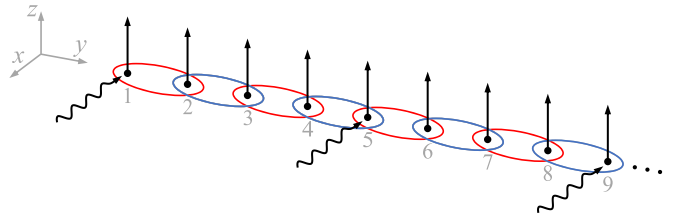


FIG. 1. A schematic figure showing the model interaction and drive protocol adapted in this work. Red (blue) color is used to denote ferro- (antiferro-) magnetic exchange in consecutive links. A stationary global field is applied in the z direction, whereas a time-periodic field in the x direction is applied at a few specific sites.

Fig. 1), we are able to control the exponential time scales of boundary relaxation characterized by the emergence of an asymptotically exact SZM. The athermal dynamics is accompanied by a rich entanglement structure of Floquet eigenstates which exhibit both thermal and athermal properties.

The rest of the paper is structured as follows. In Sec. II, we introduce our model, and discuss its symmetries and non-integrable nature. This is followed by the definition of the local Floquet protocol. In Sec. III, we discuss the boundary-driven protocol where the drive acts on a single site. Using higher-order Floquet-Magnus (F-M) expansion, we demonstrate the slow dynamics of the edge spin and the resulting properties of the approximate SZM. In Sec. IV, we give the full phenomenology of two and multi-site driving, discovering the optimal drive protocol which leads to the freezing of the boundary spin. We discuss how this novel dynamical property is accompanied by the emergence of a SZM in Sec. IV C. In order to interpret our results on the dynamics, we analyze the entanglement structures of the Floquet eigenstates in Sec. V, and show their thermal and athermal properties for specific bipartitions. Section VI summarises the salient results and their implications for athermal behavior in Floquet systems.

II. MODEL HAMILTONIAN, DRIVE PROTOCOL, AND PRELIMINARIES

A. Undriven Hamiltonian

We consider the one-dimensional “staggered” (alternating ferro-antiferromagnetic exchange interaction) nearest neighbor spin-1/2 Heisenberg model with a globally applied homogeneous magnetic field, as the undriven part of our system. Its Hamiltonian is

$$H_0 = \sum_{i=1}^{N-1} (-1)^i \mathbf{S}_i \cdot \mathbf{S}_{i+1} - h \sum_{i=1}^N S_i^z, \quad (2)$$

where i refers to a site index and $\mathbf{S}_i \equiv (S_i^x, S_i^y, S_i^z)$ is the vector comprised of the usual spin-1/2 operators, and h is the magnetic field strength. N is the number of spins and we always consider open boundary conditions (OBC). As previously mentioned elsewhere by some of us [71], the model in Eq. (2) has a long history partly due to its relevance to the Haldane spin-1 chain [73–76], which can be experimentally realized in the limit of the ferromagnetic bonds being much stronger than the antiferromagnetic ones [76,77].

For $h \neq 0$, the magnetic field term reduces the symmetry of the Hamiltonian from $SU(2)$ to $U(1)$, thus the total magnetization along the z axis ($S_{\text{tot}}^z = \sum_i S_i^z$) is conserved. A subset of $U(1)$ is the \mathbb{Z}_2 symmetry, i.e. H_0 commutes with the D_z operator, where

$$D_\alpha = \prod_{i=1}^N 2S_i^\alpha \quad (3)$$

with $\alpha = x, y, z$. In terms of spatial symmetries, H_0 is reflection symmetric (with respect to the central bond) only for even N . For odd N , H_0 is found to anticommute with the operators

$$\mathcal{A}_\alpha \equiv D_\alpha R, \quad (4)$$

for $\alpha = x, y$, where we have defined,

$$R \equiv \prod_{i=1}^{(N-1)/2} \text{SWAP}(i, N-i+1). \quad (5)$$

R is the reflection operator with respect to the central site and $\text{SWAP}(i, j)$ is the SWAP gate, defined as $\text{SWAP} \equiv |\uparrow\uparrow\rangle\langle\uparrow\uparrow| + |\uparrow\downarrow\rangle\langle\downarrow\uparrow| + |\downarrow\uparrow\rangle\langle\uparrow\downarrow| + |\downarrow\downarrow\rangle\langle\downarrow\downarrow|$. Consequently, H_0 has a spectral reflection symmetry (i.e., if there is an eigenstate $|\psi\rangle$ of energy E , then there is also an eigenstate $\mathcal{A}|\psi\rangle$ with energy $-E$) for odd N .

We find that there are exponentially many (with system size) exact zero energy states at $h = 0$ for odd N , intriguingly such a feature has also been reported in other models that harbor a superspin structure, which translates to the existence of QMBS [29, 78–82]. For any eigenstate $|\psi\rangle$ with magnetization m_z , there is always an eigenstate $R|\psi\rangle$ ($D_\alpha|\psi\rangle$, for $\alpha = x, y$) with magnetization m_z ($-m_z$). For even N , both the spectral reflection ($E \rightarrow -E$) symmetry and exact zero energy states are lost but the latter property still remain valid.

Despite its superficial resemblance to the integrable uniform Heisenberg chain, the staggered model is nonintegrable. Focusing on even N , here $N = 16$, we work in the zero-magnetization sector ($S_{\text{tot}}^z = 0$) and switch off the magnetic field at the last site to remove the presence of conventional symmetries (e.g., S^2 conservation, inversion symmetry) [83], which must otherwise be accounted for in the determination of level statistics. The middle 60% of the many-body spectrum is used for the purpose of computing level statistics, this is done to focus on properties at infinite temperature. Due to the limited statistics of eigenvalue spacings available for every bin, it is instead useful to monitor the integrated level spacing distribution,

$$I(s) = \int_0^s P(s') ds', \quad (6)$$

where $P(s')$ is the probability density of the unfolded energy level spacings (spacings divided by their mean). Note that $I(s)$ is simply the cumulative distribution function of the unfolded spacings s .

In Fig. 2, we plot $I(s)$ for the case of $h = 1$, and find that it closely resembles the results of a Gaussian orthogonal ensemble (GOE) of the random matrix theory [84], a signature

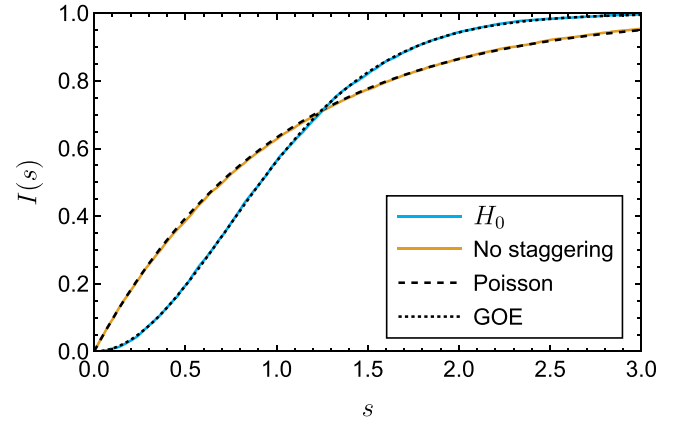


FIG. 2. Integrated level spacing distribution $I(s)$ for H_0 (in blue) and H_0 without staggering (in yellow), both with $h = 1, N = 16$. Black lines show a comparison with Poisson statistics, the signature of integrability (dashed), and GOE, valid for chaotic systems (dotted).

of chaotic, nonintegrable systems.¹ In comparison, when the bonds are made uniform (instead of staggered), we find that $I(s)$ follows the Poisson distribution, as expected for integrable models.

B. Strong zero mode

Our work here is inspired by the aim of engineering a strong zero mode, a quasilocal conserved operator, localized at the edge of a one-dimensional quantum system which gives rise to long coherence times of the edge spin [46–48, 51, 85]. The emergence of SZM is closely related to the existence of a discrete symmetry which can lead to a local conservation law on the edge of a system. Therefore characterization of the SZM operator \hat{O}_{szm} in a spin-1/2 system, described by the Hamiltonian H , requires certain algebraic properties to be satisfied which have an impact on the spectrum and dynamics of local observable [46, 47]. These properties are the following.

(1) There exists a discrete symmetry operator D in the system, i.e., $[D, H] = 0$, implying the eigenstates are split into two sectors, labeled by the eigenvalues of D .

(2) \hat{O}_{szm} anticommutes with D , $\{\hat{O}_{\text{szm}}, D\} = 0$, and therefore pairs the eigenstates between the sectors of D .

(3) \hat{O}_{szm} must be normalizable, $\hat{O}_{\text{szm}}^2 \propto \mathbb{I}$.

(4) \hat{O}_{szm} asymptotically commutes with H , i.e., $||[H, \hat{O}_{\text{szm}}]|| \sim \exp(-aN)$ with $a > 0$. A consequence of this is that \hat{O}_{szm} is a conserved quantity in the thermodynamic limit and that the gap falls off exponentially in the system size.

We, therefore, expect that a system endowed with a SZM is characterized by a spectrum-wide (quasi-)degeneracy and relaxation of the edge that can be slowed down by increasing the system size. It is also important to satisfy all these conditions simultaneously to have SZM in a system, for example, one can construct an operator which satisfies the last

¹We find similar results for $h \rightarrow 0$ i.e., even the staggered Heisenberg model without a field is nonintegrable, consistent with previous integrability tests of Ref. [118].

condition but does not correspond to a SZM. The undriven staggered Heisenberg chain (H_0) is not expected to possess a normalizable SZM and, consequently, expectation value of any edge spin operator should quickly relax to zero starting from any randomly chosen ordered state. In a bid to effectively decouple the edge spin from the rest of the system, we adopt the strategy of driving it locally with a protocol we describe next.

C. Drive protocol

Throughout this work, we adopt a Floquet drive protocol that involves applying a time-periodic magnetic field in the x direction on a subsystem that includes the boundary spin. The total time-dependent Hamiltonian is given by

$$H(t) = H_0 + f(t)V, \quad (7)$$

$$f(t) = \gamma \text{sgn}[\sin(\omega t)], \quad \text{and } V = \sum_{i \in s_d} S_i^x,$$

where $\text{sgn}(x)$ is the sign function, and thus its profile is that of a ‘‘square pulse,’’ and s_d is the set of driven sites (see Fig. 1). γ and ω are the drive amplitude and frequency, respectively and $\tau \equiv 2\pi/\omega$ is the time duration of one drive cycle. The time-averaged field in the x -direction is zero at stroboscopic times (integer number of drive cycles). We note that some aspects were previously considered for the special case of a single driven bulk site [86–88].

The time evolution operator over one drive cycle can be written as

$$U(\tau) = e^{-i(H_0 - \gamma V)\frac{\tau}{2}} e^{-i(H_0 + \gamma V)\frac{\tau}{2}} = e^{-iH_F \tau}. \quad (8)$$

Since we focus on stroboscopic dynamics, $t = n\tau$ where n is an integer, analyzing the properties of $U(\tau)$ or equivalently H_F is adequate for long time dynamics. A key contribution of our work is to explicitly derive H_F , to some approximation, in a bid to understand the exact stroboscopic dynamics seen in our numerical calculations. The explicit form of H_F was computed to the lowest order in the F-M expansion for the case of a single driven site in the bulk [71], a result we revisit in the next section for the boundary driven case.

D. Observables

Both from an experimental and theoretical point of view it is advantageous to monitor the time dependence of local operators, here we focus on $\langle \psi(n\tau) | S_i^x | \psi(n\tau) \rangle$, where

$$|\psi(n\tau)\rangle = U(n\tau)|\psi_0\rangle = U^n(\tau)|\psi_0\rangle \quad (9)$$

is the time-dependent state starting from an initial state $|\psi_0\rangle$. The initial state is typically chosen to be ‘‘simple,’’ for example, a product state in the x basis, with the hope that it can be easily realized in experiments [18,89–91].

Further theoretical insights can be obtained from the time-dependent von Neumann entanglement entropy,

$$S_A^{vN}(n\tau) = -\text{Tr}[\rho_A(n\tau) \ln \rho_A(n\tau)], \quad (10)$$

where A refers to a single site or collection of sites. The reduced density matrix of this collection of sites, ρ_A , is computed by tracing out all degrees of freedom not part of A

(labeled by \bar{A}) in the full density matrix

$$\rho_A(n\tau) = \text{Tr}_{\bar{A}}[|\psi(n\tau)\rangle\langle\psi(n\tau)|]. \quad (11)$$

In this work, we choose A to include either a single site, or a collection of driven sites. While local observables can be routinely measured in quantum simulation experiments, accessing the Rényi entanglement entropy is also feasible [92–94]. Entanglement entropy is a useful metric for distinguishing between low-entangled states (area law or lower) or those with high entanglement (typically, volume law). Thus it reveals the existence or absence of (Floquet) ETH and is also useful for the detection of QMBS [29,34].

III. BOUNDARY-DRIVEN APPROXIMATELY CONSERVED STRONG ZERO MODE

A. Overview of salient features of dynamics

Given the setup in the previous section, we study the stroboscopic relaxation of the spins when only the left boundary spin is driven, i.e., $s_d = \{1\}$. The main purpose is to explore the existence of parameters that freeze the dynamics of the edge spin via the emergence of a local conserved quantity (for example, S_1^x) which can lead to realizing a strong SZM. Instead, we find an *approximate* SZM for the boundary-driven protocol, i.e., no operator satisfies the criteria outlined previously. However, the lessons learned from understanding this case facilitate a series of drive protocols that lead us to a SZM, demonstrated in the following sections.

We summarize our key physical findings in this section, which relies on constructing H_F using a resummed F-M expansion to different levels of accuracy. First, we revisit the result for H_F to zeroth order ($l = 0$) in the F-M expansion, by transforming to the rotating frame. We show that this approximation, while qualitatively correct for many situations, fails to capture the dynamics evaluated from exact numerics near certain special drive frequencies which we dub as ‘‘freezing frequencies’’ [69]. This failure motivates the technically challenging computation of H_F to second order which contains multiple terms, we classify as ‘‘local’’ and ‘‘nonlocal.’’ We find that the local terms, treated accurately to high order in the inverse drive strength, renormalize the freezing frequency in excellent agreement with the exact results. Finally, we demonstrate that describing the slowdown of the boundary spin at and near the freezing frequencies requires the incorporation of additional nonlocal terms.

We initialize our system to a simple product state with all spins pointing along the $-x$ axis,

$$|\psi_0\rangle = |-X\rangle \equiv \bigotimes_{i=1}^N |\leftarrow\rangle_i. \quad (12)$$

In the absence of an applied magnetic field ($h = 0$), this state, being the maximally polarized ferromagnet along the $-x$ direction, is an exact eigenstate of H_0 with energy $E = 0$ for odd N and $E = 1/4$ for even N . When decomposed in terms of S_{tot}^z projected eigenstates, we get

$$|\psi_0\rangle = \frac{1}{2^{N/2}} \sum_{r=0}^N \sqrt{N C_r} \left| S_{\text{tot}}^z = \frac{2r - N}{2} \right\rangle. \quad (13)$$

When a nonzero z field ($h \neq 0$) is turned on, the projected S_{tot}^z states (on the right-hand side) remain eigenstates of H_0 , but their degeneracy is split. Thus $|\psi_0\rangle$ no longer remains an eigenstate of H_0 . These projected states were shown to have low entanglement [34], in violation of the expected volume law at infinite temperature. Thus this state serves as perhaps the simplest example of an embedded superspin (at high energy) in an otherwise chaotic spectrum, this is the basic idea at the core of perfect QMBS [34,95].

Though the system initialized with $| -X \rangle$ exhibits perfect oscillations (in the Loschmidt echo and various observables) under the action of H_0 , the situation is starkly different when the system is subject to a local periodic drive [Eq. (7)]. In previous work [71], we found that there are at least two parametric regimes depending on the kick strength and frequency. Typically, the driven spin thermalizes collectively with the rest, however, when a freezing condition involving the drive strength and frequency is satisfied, the driven spin is almost (but not strongly) decoupled from the rest of the system. We will elaborate on this in the next subsection.

In what follows, we have worked primarily with the $| -X \rangle$ initial state, however, we emphasize that all our results remain insensitive to this choice and are valid for any product state in the S^x basis.

B. Failure of the zeroth order Floquet Hamiltonian

We perturbatively construct and analyze the Floquet Hamiltonian, H_F , using a resummed F-M expansion (as charted out in detail in Appendix A). In this scheme, $H_F = \sum_{l=0}^{\infty} H_F^{(l)}$ where the various orders are denoted by $H_F^{(l)}$ and, in principle, can be calculated for each l .

A computation of the $l = 0$ term gives

$$\begin{aligned} H_F^{(0)} = & -S_1^x S_2^x - \frac{\sin \lambda}{\lambda} (S_1^y S_2^y + S_1^z S_2^z) \\ & + \frac{1 - \cos \lambda}{\lambda} (S_1^z S_2^y - S_1^y S_2^z) \\ & - \frac{h}{\lambda} [\sin \lambda S_1^z + (1 - \cos \lambda) S_1^y] \\ & + \sum_{i=2}^{N-1} (-1)^i \mathbf{S}_i \cdot \mathbf{S}_{i+1} - h \sum_{i=2}^N S_i^z, \end{aligned} \quad (14)$$

where $\lambda \equiv \gamma\tau/2 = \pi\gamma/\omega$. Additionally, the calculation for $l = 1$ shows that $H_F^{(1)}$ vanishes for all drive parameters.

When $\lambda = 2\pi k$, where k is an integer, the only nonzero term involving the driven boundary site in H_F (calculated up to $l = 1$) is $-S_1^x S_2^x$. This suggests that the edge spin can be *completely frozen* if one tunes the drive frequency to $\omega_c^k = \gamma/(2k)$ since the following commutation relation

$$[S_1^x, H_F^{(0)} + H_F^{(1)}] = 0 \quad (15)$$

is exactly satisfied.

We focus on the $k = 1$ case, though all the discussions remain valid for any k . Figure 3(a) presents the stroboscopic dynamics of S_i^{vN} , for all i with $s_d = \{1\}$. We find that the relaxation rate of the boundary spin is indeed very small at $\omega \sim \omega_c^k$ (compared to other sites which thermalize very quickly in spite of being undriven), however, it is always nonzero.

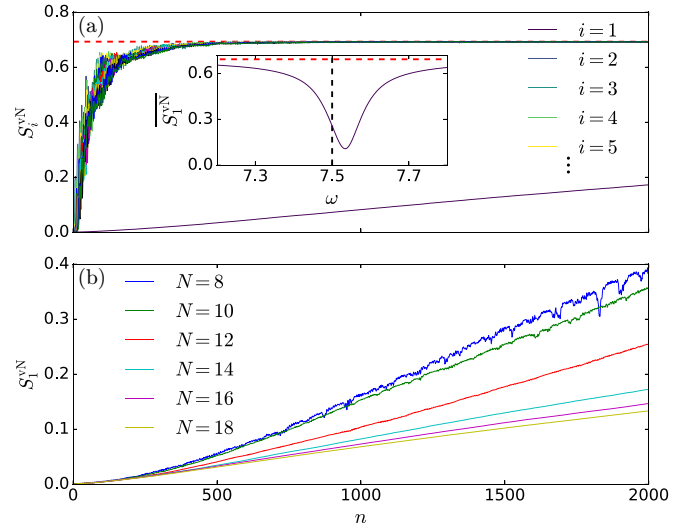


FIG. 3. Stroboscopic dynamics of (a) single site entanglement entropy S_i^{vN} for all the sites (i) for $N = 14$. The red (dashed) line is used to denote the maximum single-site entropy ($\ln 2$). $\overline{S_1^{vN}}$ (averaged S_1^{vN} over first 2000 cycles) is plotted with ω in the inset showing the absence of dynamic freezing of the edge spin even for the most appropriate choice of the drive frequency. A vertical dashed line is also drawn at $\omega_c^1 = 7.5$ to clearly show the minima in $\overline{S_1^{vN}}$ (ω_m^1) is shifted from ω_c^1 . (b) entanglement entropy of the boundary site (S_1^{vN}) for different system sizes (N). $h = 1$, $\gamma = 15$, and $\omega = \omega_m^1 = 7.53$ for both the panels. The $N = 16$ and $N = 18$ calculations were done with matrix-product-state-based TEBD calculations for a time step of $\delta t = \tau/100$ and a maximum bond dimension of $2^{N/2}$.

This can be seen in the inset of Fig. 3(a), where we plot S_1^{vN} averaged over the first 2000 cycles with ω near ω_c^1 . The frequency which gives the slowest relaxation ($\omega = \omega_m^k$) shifts to a somewhat higher value compared to ω_c^k (i.e. $\omega_m^k > \omega_c^k$). This result can not be explained by the lowest-order ($l = 0$) Floquet Hamiltonian.

We also monitor the size dependence of the relaxation rate of S_1^{vN} in Fig. 3(b) using a combination of exact diagonalization for $N \leq 14$, and matrix product state based time-evolving block decimation (TEBD) technique [96,97] for $N > 14$, setting the bond dimension to its maximal value of $2^{N/2}$. A second-order Trotter decomposition with a time step of $\delta t = \tau/100$ was used for the TEBD calculations [98], we checked there was almost no difference in our results in the range $\delta t = \tau/30$ to $\delta t = \tau/100$. While increasing the system size, we find that the relaxation of the edge spin slows down, but not exponentially in system size. Moreover, the relaxation dynamics tends to be saturated beyond a threshold system size [≈ 16 as can be seen in Fig. 3(b)], an observation that is consistent with the phenomenology of an approximate SZM [47].

C. Higher order corrections and freezing condition

To explain our numerical observations, we need to go to higher terms in the F-M expansion. However, before we dive into this calculation, we note that the F-M expansion to obtain the Floquet Hamiltonian for interacting systems is plagued by various convergence issues [56].

Though these issues can be circumvented to some extent by systematic resummations in certain parameters (e.g. drive frequency) [59,99,100], the calculation of the resummed expansion becomes increasingly difficult in higher order in other parameters (e.g., drive amplitude) due to the presence of nested commutators of many-body terms. In spite of this, the calculation of higher-order terms in F-M has been fruitful, as it can reveal physical effects not accessible in the lower order expansion.

As anticipated, the calculation of $H_F^{(2)}$ is somewhat complicated by the existence of multiple terms, for completeness the various contributions have been described in Appendix A. Here we categorize the resulting expression into “local” and “nonlocal” parts,

$$H_F^{(2)} = H_{F, \text{loc}}^{(2)} + H_{F, \text{nonloc}}^{(2)}. \quad (16)$$

The “local” part, consisting of only one- and two-body (n.n.) operators (including the boundary site), can be written as

$$H_{F, \text{loc}}^{(2)} = a_1(\mathbf{p})S_1^z + a_2(\mathbf{p})S_1^y + a_3(\mathbf{p})S_1^z S_2^z + a_4(\mathbf{p})S_1^y S_2^y + a_5(\mathbf{p})S_1^z S_2^y + a_6(\mathbf{p})S_1^y S_2^z + \dots, \quad (17)$$

where $\mathbf{p} \equiv (h, \gamma, \tau)$ represents the set of drive parameters (see Appendix A for the full expression of all the a_i coefficients). The ellipsis denotes terms, which commute with S_1^x . It is important to note that our classification of “local” is based on the fact that the terms have the same functional forms as those appearing in $H_F^{(0)}$, hence only renormalizing their strength.

Interestingly, we find that a_i s contain terms with similar magnitude as the zeroth ($l = 0$) term [i.e. $\mathcal{O}(1/\gamma)$], some of which can be nonzero even at the special freezing frequencies ω_c^k . Collecting only the $\mathcal{O}(1/\gamma)$ terms from $H_{F, \text{loc}}^{(2)}$, we rewrite H_F as

$$\begin{aligned} H_{F, \text{loc}} \left[\mathcal{O}\left(\frac{1}{\gamma}\right) \right] &= H_F^{(0)} + H_F^{(1)} + H_{F, \text{loc}}^{(2)} [\mathcal{O}(1/\gamma)] \\ &= -S_1^x S_2^x - \frac{2 \sin \lambda}{\gamma \tau} \left[\left(1 + \frac{(1 + 4h^2)\tau^2}{48}\right) S_1^y S_2^y + \left(1 + \frac{\tau^2}{48}\right) S_1^z S_2^z \right] \\ &\quad + \frac{2}{\gamma \tau} \left[\left(1 - \cos \lambda - \frac{(1 + 4h^2)\tau^2(2 + \cos \lambda)}{48}\right) S_1^z S_2^y - \left(1 - \cos \lambda - \frac{\tau^2(2 + \cos \lambda)}{48}\right) S_1^y S_2^z \right] \\ &\quad - \frac{2h}{\gamma \tau} \left[\sin \lambda \left(1 + \frac{\tau^2}{48}\right) S_1^z + \left(1 - \cos \lambda - \frac{\tau^2(2 + \cos \lambda)}{48}\right) S_1^y \right] + \sum_{i=2}^{N-1} (-1)^i \mathbf{S}_i \cdot \mathbf{S}_{i+1} - h \sum_{i=2}^N S_i^z. \end{aligned} \quad (18)$$

With this expression it becomes clear that $[S_1^x, H_F] \neq 0$ at $\omega = \omega_c^k$. In fact, there is not a single \mathbf{p} for which all S_1^x noncommuting terms in Eq. (18) simultaneously go to zero. In other words, it is impossible to dynamically freeze the edge spin via the emergence of a corresponding local conserved quantity. This result must be contrasted with the case of global driving with a square pulse [69], where the terms in $H_F^{(2)}$ are expected to be at least $\mathcal{O}(1/\gamma^2)$ or smaller (see Appendix C).

The local terms, to order $1/\gamma$, do not significantly affect the freezing condition obtained from $H_F^{(0)}$, they alone are quantitatively inadequate for explaining the observed shift in the freezing frequency. Thus we retain higher order local terms in $H_{F, \text{loc}}^{(2)}$ and define

$$H_{F, \text{loc}} \left[\mathcal{O}\left(\frac{1}{\gamma^3}\right) \right] \equiv H_F^{(0)} + H_F^{(1)} + H_{F, \text{loc}}^{(2)} \left[\mathcal{O}\left(\frac{1}{\gamma^3}\right) \right]. \quad (19)$$

To demonstrate that the Hamiltonian in Eq. (19) captures the shift of the point of minimum relaxation to a frequency slightly higher than ω_c^k , we calculate a matrix element of H_F in the S^x -basis, $H_F(2, 1)$ where $|1\rangle = |\psi_0\rangle$ and $|2\rangle = \sigma_1^z |1\rangle$. Figure 4 shows a comparison of different levels of approximation for $H_F(2, 1)$ with the exact numerical calculation. One can see that $|H_F(2, 1)|$ obtained from Eq. (18), though always nonzero (supporting the absence of freezing of the edge spin), does not match the exact results, particularly it still shows the minimum at a frequency which is extremely close to ω_c^k , rather than the shifted value. In comparison, including the local $\mathcal{O}(1/\gamma^2)$ and

$\mathcal{O}(1/\gamma^3)$ terms in $H_F^{(2)}$ yields substantially good agreement with the exact numerics, in particular the location of the minima of matrix elements [like $H_F(2, 1)$] which determines the freezing frequency.

Going beyond individual matrix elements, we compare the exact stroboscopic dynamics with that generated by the $H_{F, \text{loc}}[\mathcal{O}(1/\gamma^3)]$ in Fig. 5. This approximation is excellent for capturing the dynamics of all spins away from the freezing frequency. At and near the freezing frequency, it captures the dynamics of all, but the boundary spin, accurately. Thus the local H_F approximation can capture not only the individual matrix elements but also the stroboscopic dynamics quite accurately at least for short times.

D. Role of nonlocal terms to slowdown the edge spin

Interestingly, the failure of the local $H_F^{(2)}$ only for the dynamics of the boundary spin at and near ω_m^k reveals the importance of the nonlocal terms, that we have ignored up to this point. We have numerically checked that near the freezing frequency many matrix elements of H_F , generated by long-range and multi-spin interaction terms involving the boundary spin are significant relative to the local matrix elements [like $H_F(2, 1)$ which shows a minimum at this parameter regime]. We find that such nonlocal terms, appearing in $H_F^{(2)}$, can at most be four-body operators having support on sites 1–4. We have calculated all such terms (dubbed as $H_{F, \text{nonloc}}^{(2)}$) with

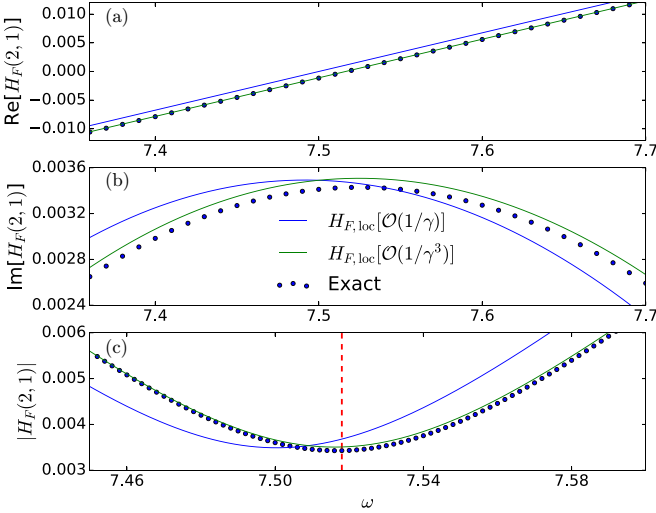


FIG. 4. Comparison of (a) real, (b) imaginary, and (c) absolute values of $H_F(2, 1)$ between exact numerics (black dots) and expressions obtained from F-M expansions. Blue (green) curve is obtained from Eq. (18) [Eq. (19)]. A vertical red (dashed) line is used in (c) to guide the eye to the minima of $H_F(2, 1)$ which is clearly shifted from $\omega_c^1 = 7.5$. $h = 1$, $\gamma = 15$, and $N = 8$.

their respective strengths in terms of the drive parameters (see Appendix A). Such terms when included in H_F are found to improve the agreement with exact numerics for the boundary spin [see Fig. 5(b)].

The nonlocal terms, though very weak, will proliferate in further higher orders; a careful inclusion of them may increase the timescale of the agreement with exact numerics. In fact,

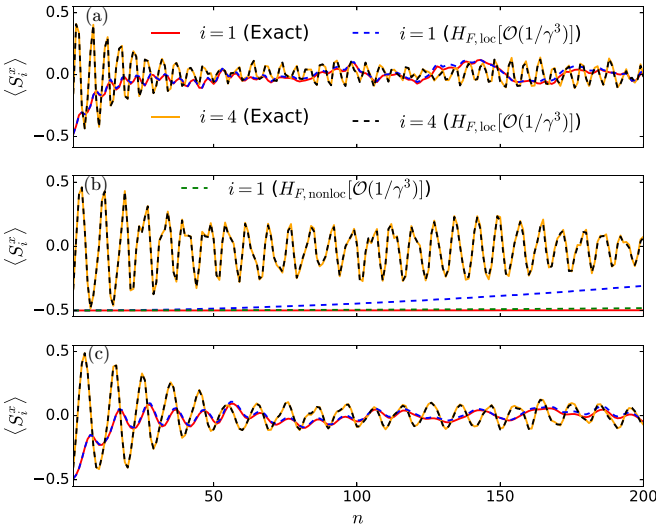


FIG. 5. Comparison of stroboscopic dynamics from exact numerics and analytical H_F obtained from the resummed F-M expansion at (a) $\omega = 5$ (b) $\omega = 7.53$ (c) $\omega = 10$. $\gamma = 15$, $h = 1$, and $N = 8$. Away from the freezing frequency the stroboscopic dynamics is well captured for all spins within a “local” approximation for H_F , in comparison to exact numerics. At or near the freezing frequency, nonlocal terms are required to accurately capture the behavior of the driven boundary spin.

we find that the nonlocal and multisite terms already present in $H_{F,\text{nonloc}}^{(2)}$ are sufficient to capture the slow dynamics of the edge spin accurately up to $n \sim 200$. The strength of the nonlocal terms calculated in second order ($l = 2$) is renormalized in higher order in the F-M expansion which in turn extends the agreement with exact dynamics to longer times. This is quite nontrivial for two reasons. First, any nonthermal (or prethermal) phenomenon in a Floquet system is naively expected to be linked with the existence of a local H_F whereas a nonlocal H_F usually promotes heating. But here we observe the exact opposite, the thermalizing dynamics of the bulk sites is well captured by a local H_F (even at ω_m^k as shown in Fig. 5) but not the freezing dynamics of the boundary site which necessitates the presence of certain long-range terms for its onset. Here we also note that $H_{F,\text{nonloc}}^{(2)}$ is completely off-diagonal in the x basis and the proliferation of these terms is expected to dephase the initial state $|\psi_0\rangle$. Second, from a practical point of view, it establishes the freezing phenomenon reported in this work as a genuine drive-induced many-body effect, which is challenging to engineer with fine-tuned long-range terms in a time-independent Hamiltonian.

As noted previously, the rate of relaxation of the boundary spin at the special frequencies (ω_m^k) decreases further with increasing system size, as can be seen in Fig. 3(b). This is at odds with the usual expectation that increasing the system size generically increases the phase space available for thermalization and should thus speed up the process. This apparent anomalous behavior already suggests that boundary driving alone can be enough to trigger the onset of an approximate SZM [47,50] in the system. However, the relaxation time of the boundary spin is significantly shorter than the time associated with a SZM, in which case it is exponentially large in system size.

The inability of boundary-site driving to fully freeze the boundary spin and the presence of nonlocal terms motivates the next natural question: what happens when multiple sites (including the boundary one) are driven together? Is there any requirement on the number of driven sites as well as the specific locations where the drive should be applied to maximize the lifetime of the edge spin? We address these questions in the next section.

IV. EMERGENCE OF THE STRONG ZERO MODE VIA MULTISITE DRIVING

A. Optimal drive protocol

We now consider a situation when multiple spins in the bulk are driven simultaneously, in addition to the boundary. Intuitively, the increase in the number of driven sites would lead to more rapid thermalization of all the spins. As discussed in Sec. III D, each driven site generates a larger collection of nonlocal terms which slow down the edge spin near the freezing frequency. In this section, we first explore the landscape of few-site protocols and investigate their effects on the edge spin. This subsequently leads us to the development of a multi-site driving protocol, resulting in the further slowdown of the edge spin.

When the boundary and a generic bulk site are driven together, our results indicate that the relaxation of the boundary

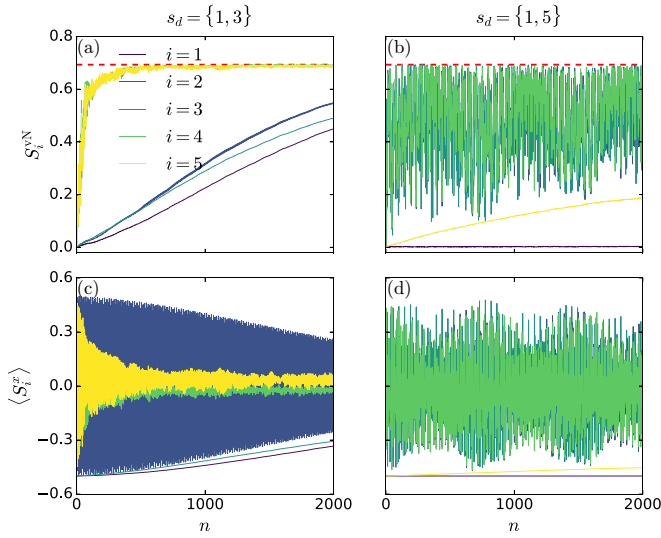


FIG. 6. Stroboscopic S_i^{vN} (top) and $\langle S_i^x \rangle$ (bottom) for different two-site driving. Locations of the driven sites (s_d) are mentioned at the top of each column. $h = 1$, $\gamma = 15$, $\omega = \omega_m^1 = 7.53$, and $N = 14$.

spin gets faster. We demonstrate this behavior with an example for $s_d = \{1, 3\}$ in Figs. 6(a) and 6(c), where we observe that the relaxation of the boundary site is faster than the case of $s_d = \{1\}$. The undriven sites are found to thermalize quickly, with the exception of the intermediate spins, which exhibit slower relaxation to thermal equilibrium. However, remarkably we find that a particular two-site driving protocol results in strong freezing of the edge spin: when in addition to the boundary site the fifth site is also driven ($s_d = \{1, 5\}$). Indeed, the first site shows almost no relaxation of $\langle S_1^x \rangle$ for the drive cycles plotted in Figs. 6(b) and 6(d). The intermediate sites assume a different character now, showing a strong temporal oscillation before eventually decaying out to zero. This particular driving protocol also causes a widened frequency window which admits slow (but nonzero) relaxation of the edge spin. Moreover, we find that the relaxation of the edge spin, analogous to the boundary-driven case, slows down with increasing the system size (see the inset in Fig. 7).

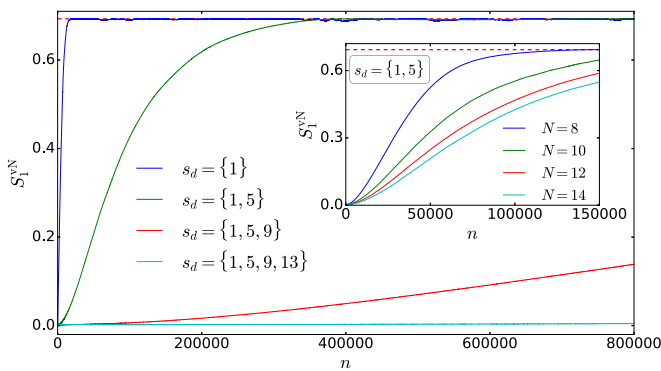


FIG. 7. Long time stroboscopic dynamics of S_1^{vN} for different multi-site driving showing the optimal choice of drive locations (every fourth site) to freeze the boundary spin. Inset shows S_1^{vN} vs n for $s_d = \{1, 5\}$ for different system sizes. All parameters are the same as in Fig. 6.

This freezing behavior is necessarily a high-order many-body effect, as the drive itself only produces interactions with a range of three sites away from the driven one (in the second term in F-M). Therefore driving site 5 does not change the structure of the effective Hamiltonian from Eq. (18), only adding terms supported on sites 2–8. This implies that the origin of the suppression of the boundary relaxation is a higher-order many-body process, where the driven site 5 impacts sites 2–4, which in turn impact the boundary. This complex collective behavior seems to be a unique property of only this particular two-site protocol ($s_d = \{1, 5\}$), and will become the key ingredient in our subsequent proposal for the Floquet engineering of the SZM.

We also note that the additional driven site is itself not frozen. This can be understood by noticing that the Hamiltonian now includes newly generated three-body interaction terms (e.g., $S_4^x S_5^z S_6^x$, see Appendix B), which renormalizes the field strength at site 5. Note that such a term cannot occur for the boundary-driven case. To illustrate this one can, for example, compare the aforementioned matrix element $H_F(2, 1)$ with the matrix element representing single spin-flip events at site 5, $\langle \psi_0 | H_F \sigma_5^z | \psi_0 \rangle$. Indeed, we find the latter to be larger in magnitude, contributing to a much faster dephasing of site 5 as compared to site 1.

B. Freezing of edge spin on increasing the number of driven sites

Motivated by our observation of the slowdown of the edge due to the two-site protocol, we consider the driving of additional sites. Increasing the number of driven sites further, we find that generically there is a rapid relaxation of all sites, including the boundary. However, when the driving sequence is specifically chosen as $s_d = \{1, 5, 9\}$, the freezing of the boundary site is significantly enhanced compared to the two-site protocol with $s_d = \{1, 5\}$. We can conclude that the further slowdown has a similar origin to the two-site protocol: a high-order many-body process, this time involving site 9. Based on the spatial periodicity of the few-site protocols, we propose the following Floquet engineering protocol to further slowdown the edge spin, where the driving sequence is composed of the cluster $s_d = \{1, 5, 9, \dots, 4k + 1\}$. Subsequently, we will use the term “every fourth site” to describe this cluster, and designate the total number of driven sites as $n_d^{4\text{th}}$. The existence of this protocol does not preclude other protocols which can stabilize a SZM, and we consider this as a particular case in a general class of locally driven protocols.

In Fig. 7, we show how the growth of entanglement entropy of the boundary site decreases while increasing the size of the cluster s_d : we find a hierarchy of freezing behaviors with the growing number of driven spins. This conclusion is supported by the exact diagonalization results allowing us to reach large number of drive cycles, see Fig. 7. Furthermore, the inset in Fig. 7 shows that although increasing the system size alone improves the freezing behavior, the slowdown can be most effectively achieved by also increasing the number of driven sites.

Intuitively, the extremely slow dynamics in the proposed protocol is directly related to the gaps between quasienergy levels in the Floquet spectrum. This can be seen by considering thermalization of the expectation value of a local

observable for a driven state $|\psi(n\tau)\rangle$ [101–103]:

$$\begin{aligned} \langle \psi(n\tau) | S_1^x | \psi(n\tau) \rangle &= \sum_{q \neq r} c_r^* c_q e^{i(\epsilon_r - \epsilon_q)n\tau} \langle \Phi_r | S_1^x | \Phi_q \rangle \\ &+ \sum_r |c_r|^2 \langle \Phi_r | S_1^x | \Phi_r \rangle, \end{aligned} \quad (20)$$

where ϵ_r and $|\Phi_r\rangle$ are the r th quasienergy and eigenstate in the first Floquet Brillouin zone (BZ). The first sum in the equation controls the relaxation speed, while the second sum gives the long-time expectation value in the thermalized state (diagonal ensemble average). For our protocol, the zeroth-order effective Floquet Hamiltonian $H_F^{(0)}$ along with the second-order corrections, are invariant under $S^x \rightarrow -S^x$ transformation, which constraint the diagonal ensemble average of S_1^x to be zero. Since our exact calculation of the expectation values of S_1^x in Floquet eigenstates also yield zero up to machine precision for a wide range of parameters, the invariance is expected to exist at all orders of H_F . In fact, for the general case of $s_d = \{1, 5, 9, \dots, 4k + 1\}$, correlations involving odd number of spins from the sites $4k + 1$, such as $\langle S_1^x \rangle$, $\langle S_1^x S_5^x S_9^x \rangle$, etc., are all zero.

For generic nonintegrable systems the off-diagonal contribution decays to zero quite rapidly. However here, we find that the energy gaps between the states (say r and q) which dominate the matrix elements are extremely small. For those states $|\epsilon_r - \epsilon_q|$ ranges from $\sim 10^{-5}$ for $s_d = \{1, 5\}$ dropping to $\sim 10^{-8}$ for $s_d = \{1, 5, 9, 13\}$. This is further supported by the level statistics of the Floquet Hamiltonian, which shows a strong Poisson distribution and the absence of level repulsion, putatively indicating the emergence of a symmetry or fragmentation of the Hilbert space (see Appendix D). We provide a coherent analysis of this extensive quasidegeneracy throughout the entire Floquet spectrum, which shows that the freezing ultimately has its origin in the emergence of the SZM.

C. Emergence of the strong zero mode

In this section, we elucidate the step-by-step emergence of the strong zero mode which is the crux of the exponentially slow dynamics of the edge mode operator. We expect that a system endowed with a SZM, as defined in Sec. II B, is characterized by a spectrum-wide (quasi)-degeneracy and relaxation of the edge that can be slowed down by increasing the system size.

First, let us consider the existence of a discrete symmetry operator. The undriven system has a \mathbb{Z}_2 symmetry of $D_z = \prod_i \sigma_i^z = \prod_i (2S_i^z)$, yet the drive in the x direction generally destroys it. However, we can exploit the freedom in the driving parameters and note that near the special frequencies ω_m^k the terms in Eq. (18) that do not commute with D_z vanish. We test this for the full Floquet Hamiltonian numerically in Fig. 8(a), where we plot $|\langle D_z \rangle| = \sum_{r=1}^{2^N} |\langle \Phi_r | D_z | \Phi_r \rangle| / 2^N$; this quantity approaches 1 when each Floquet eigenstate is simultaneously an eigenstate of the proposed symmetry operator. We find that although D_z is not an exact symmetry, it is nearly conserved at the special freezing frequencies. The formation of SZM requires a special pairing structure of the Floquet eigenstates and quasidegenerate eigenvalues, along with the global discrete symmetry D_z .

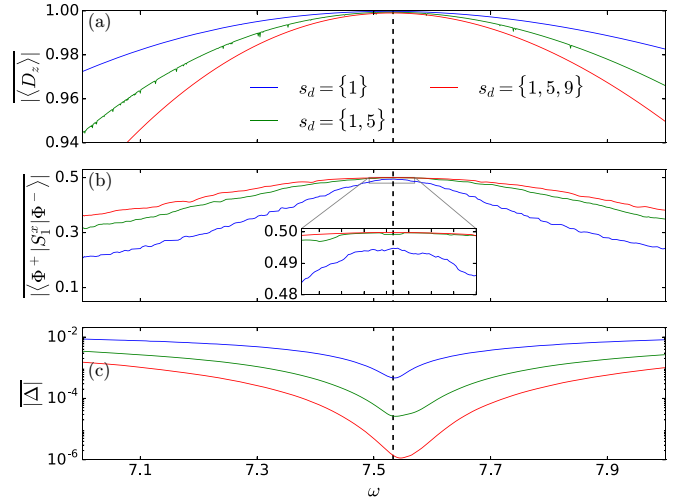


FIG. 8. Emergence of strong zero-mode: (a) $|\langle D_z \rangle|$ vs ω showing the emergence of a discrete symmetry, $D_z = \prod_i (2S_i^z)$, at $\omega \sim \omega_m^1$. (b) $|\langle \Phi^+ | S_1^x | \Phi^- \rangle|$ vs ω . Inset shows that the condition $S_1^x | \Phi^\pm \rangle = \frac{1}{2} | \Phi^\mp \rangle$ is satisfied better for $s_d = \{1, 5\}$ and $s_d = \{1, 5, 9\}$ compared to $s_d = \{1\}$. (c) $|\Delta|$ vs ω showing a deep at $\omega \sim \omega_m^1$ which implies the emergence of SZM induced quasidegeneracy between the Floquet eigenvalues from different D_z sectors. $N = 10$, $\gamma = 15$ for all the plots. We have performed a moving average over the raw data (in an ω interval of 0.008) for panel (b). The vertical dashed line is a guide to the eye to the position of strongest freezing.

We now label the Floquet eigenstates by the eigenvalues of the symmetry operator D_z as $H_F | \Phi_r^\pm \rangle = \epsilon_r^\pm | \Phi_r^\pm \rangle$. We show that the eigenstates occur in pairs in the Floquet spectrum where the operator which toggles between the states $|\Phi_r^+\rangle$ and $|\Phi_r^-\rangle$ is localized at the edge. This operator anticommutes with the global symmetry operator D_z . We propose that an approximate operator, which satisfies these properties, is $O_{\text{szm}} \approx S_1^x$. This is shown by the numerical calculation of the matrix elements of S_1^x between $|\Phi_r^+\rangle$ and $|\Phi_r^-\rangle$. In Fig. 8(b), the average matrix element over all pairs of eigenstates

$$|\langle \Phi^- | S_1^x | \Phi^+ \rangle| = \sum_{r=1}^{2^{N-1}} |\langle \Phi_r^- | S_1^x | \Phi_r^+ \rangle| / 2^{N-1}, \quad (21)$$

is plotted as a function of ω . This quantity measures how S_1^x connects the two symmetry sectors, and should approach $1/2$ when the pairing is exact. Indeed, we find that increasing the number of driven sites leads to a more accurate pairing of the states. We propose an ansatz for the Floquet eigenstates with the following structure:

$$|\Phi_r^\pm\rangle = \frac{1}{\sqrt{2}} (|\rightarrow\rangle \otimes |\xi_r^\pm\rangle \pm |\leftarrow\rangle \otimes |\bar{\xi}_r^\pm\rangle), \quad (22)$$

where states $|\xi_r^\pm\rangle$ and $|\bar{\xi}_r^\pm\rangle$ obey conditions $\langle \xi_r^\pm | \xi_q^\pm \rangle + \langle \bar{\xi}_r^\pm | \bar{\xi}_q^\pm \rangle = 2\delta_{rq}$, $\langle \xi_r^\pm | \xi_r^\pm \rangle = \langle \bar{\xi}_r^\pm | \bar{\xi}_r^\pm \rangle = 1$, and $\langle \xi_r^- | \xi_r^+ \rangle = \langle \bar{\xi}_r^- | \bar{\xi}_r^+ \rangle = \mathcal{R}_r e^{i\theta_r}$ with $\mathcal{R}_r \leq 1$ and $\theta_r \in [0, 2\pi)$. This is a general ansatz of entangled states between the edge spin and the rest of the system with the edge spin constrained to satisfy $\langle S_1^x \rangle = 0$. The structure of entanglement between them is encoded in the overlap properties of $|\xi_r^\pm\rangle$ and $|\bar{\xi}_r^\pm\rangle$, which will be highlighted in Sec V.

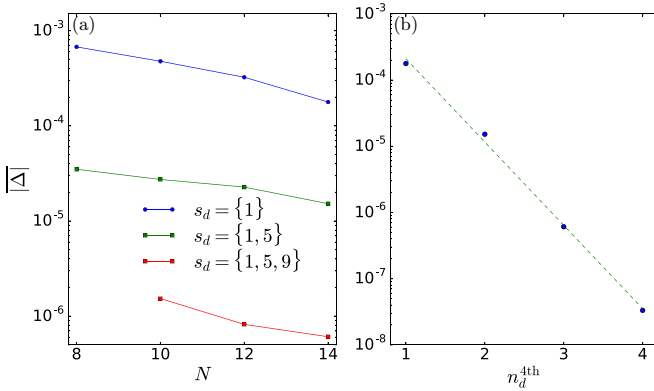


FIG. 9. Scaling of averaged pairing gaps ($|\overline{\Delta}|$) (a) with system size (N) for a fixed number of driven sites and (b) with increasing the size of the driven cluster n_d^{4th} for a fixed system size ($N = 14$). All other parameters are the same as in Fig. 6. The dashed green line in subfigure (b) is a best-fit curve to an exponential ansatz, $|\overline{\Delta}| \sim \exp(-2.9n_d^{4th})$.

These states can be utilized to encode the SZM operator with S_1^x as the leading order term.

$$\hat{O}_{\text{szm}} = \sum_r \frac{e^{i\theta_r}}{2} |\Phi_r^+\rangle \langle \Phi_r^-| + \text{h.c.} \propto S_1^x + \text{corrections}, \quad (23)$$

The corrections to the leading order term are controlled by the extent of deviation from the complete overlap between $|\xi_r^+\rangle$ and $|\xi_r^-\rangle$ states. Despite the rapid thermalization in the bulk, on increasing the cluster of driven sites we find a proliferation of the number of Floquet eigenpairs satisfying the condition $\mathcal{R}_r \approx 1$, $\forall r$ (see Appendix E). Therefore the form of the strong zero mode is indeed well-approximated by Eq. (23). The existence of this normalizable operator explains the quasidegeneracy present in the spectrum and relates it directly to the pairing of Floquet eigenstates.

Finally, we turn our attention to the commutation properties of \hat{O}_{szm} with the Floquet Hamiltonian. The commutator assumes the following form in terms of eigenstates and eigenvalues of H_F ,

$$[H_F, \hat{O}_{\text{szm}}] = \sum_r (\epsilon_r^+ - \epsilon_r^-) \frac{e^{i\theta_r}}{2} |\Phi_r^+\rangle \langle \Phi_r^-| - \text{H.c.}, \quad (24)$$

which implies that all spectral gaps must simultaneously vanish exponentially with N for the SZM to be a quasiconserved operator. In Fig. 8(c), we present results for the average pairing gap

$$|\overline{\Delta}| = \sum_{r=1}^{2^{N-1}} |\epsilon_r^+ - \epsilon_r^-| / 2^{N-1}, \quad (25)$$

where indeed the gap decreases significantly with increasing size of the driven cluster (n_d^{4th}) in the proximity of the freezing frequency. Interestingly, when we fix n_d^{4th} and start increasing the system size, the gap decreases weakly with N [see Fig. 9(a)]. We associate this slow decay of $\Delta(N, n_d^{4th})$ with N to the convergence properties of the corrections in Eq. (23), which appear to converge for smaller N , with $||[H_F, \hat{O}_{\text{szm}}]||$ decreasing in magnitude. Subsequently for larger N the cor-

rections dominate \hat{O}_{szm} with the norm of the commutator saturating to a finite value signaling the presence of an approximate SZM (as witnessed previously for the boundary driven case in Sec. III). On the other hand, if the system size is fixed, the gap exhibits an exponential fall with n_d^{4th} as shown in Fig. 9(b) (see Appendix F for more details). This leads to an exponential enhancement of the finite radius of convergence of an approximate SZM, making it an exact SZM in the thermodynamic limit. This behavior of the pairing gap explains our results for the freezing dynamics of the boundary site in Fig. 7, where we found a similar dependence of the relaxation times on the system size and the driven cluster size. Therefore we conclude that increasing both N and n_d^{4th} leads to an asymptotic exponential decrease of the average pairing gap and hence the commutator of \hat{O}_{szm} with the Floquet Hamiltonian when n_d^{4th} scales linearly with N .

In summary, we have demonstrated that the protocol involving driving every fourth site in the chain leads to the emergence of a SZM. We have proposed an approximate form of an operator that satisfies all the features of SZM which is directly related to the spectrum-wide quasidegeneracy and slow relaxation rate of the boundary spin. We note that any bulk site can not be frozen in this manner which suggests that a strictly convergent SZM, localized in the bulk, can not be constructed.

V. ENTANGLEMENT STRUCTURE OF FLOQUET EIGENSTATES

In this section, we discuss the nonequilibrium properties of the system through the lens of the entanglement entropy of Floquet eigenstates. The athermal and thermal behavior represented in the dynamics and spectral properties of the boundary and bulk degrees of freedom respectively, have an imprint on the entanglement features of the eigenstates as well. In fully thermal eigenstates at infinite temperature, the reduced density matrix of any subsystem exhibits maximal entanglement. The disentangling nature of the periodic drive introduces several novel features in entanglement which we categorize between thermal and athermal depending on the partitioning of subsystems.

The von Neumann entanglement entropy of the boundary site with the rest of the system in the Floquet eigenstates (22) can be written as

$$S_1^{\text{vN}, \pm} = -\frac{1 + |\delta^\pm|}{2} \ln \frac{1 + |\delta^\pm|}{2} - \frac{1 - |\delta^\pm|}{2} \ln \frac{1 - |\delta^\pm|}{2}, \quad (26)$$

where $\delta_r^\pm = \langle \xi_r^\pm | \xi_r^\pm \rangle$. In the protocol with $s_d = \{1\}$, $|\delta_r^\pm|$ is found to be large for many eigenstates, thus giving rise to many weakly entangled states, nonetheless in a large majority of states the edge spin remain maximally entangled with the bulk as shown in Fig. 10(a). In the other limit, for $s_d = \{1, 5, 9, 13\}$ the boundary spin is maximally entangled in all the Floquet eigenstates [see Fig. 10(b)] which also implies $|\delta_r^\pm|$ is vanishingly small. This is counterintuitive since, the enhanced freezing of the boundary spin is expected to lead to disentangling of the edge spin in the Floquet eigenstates, which instead appears fully ergodic for single-site observables. This means that though the boundary spin takes an

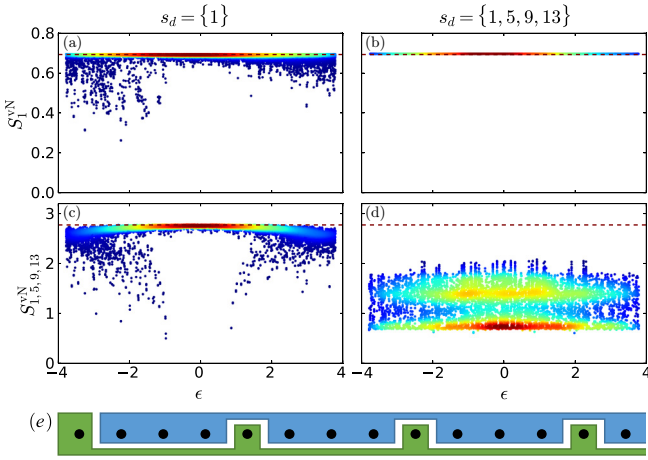


FIG. 10. Entanglement entropy of the boundary site with the rest of the system (S_1^{vN}) in the upper panels, and sites $\{1,5,9,13\}$ with the rest of the system ($S_{1,5,9,13}^{vN}$) in the lower panels for $N = 14$. The driven sites are mentioned at the top of each column. All other parameters are the same as in Fig. 6. Page values of entanglement entropies are shown by the red dashed line. The bipartition used to calculate the entanglement entropy in (c) and (d) is shown in (e).

exponentially long time in N to dephase, it should finally reach a featureless state for any finite system size. Therefore the dynamics of the boundary spin, however slow it may be for finite systems, is a type of prethermal phenomenon with anomalously long (exponential in system size instead of some large but fixed parameter strength) thermalization time.

However, the scaling of the averaged gap between the Floquet eigenpairs in Fig. 9 suggests that it should vanish in the thermodynamic limit. Consequently, the decoherence time of the boundary spin diverges as well as the states $|\Phi_r^+\rangle$ and $|\Phi_r^-\rangle$ become degenerate. This will allow us to choose $(|\Phi_r^+\rangle \pm |\Phi_r^-\rangle)/\sqrt{2}$ as the Floquet eigenstates, where the boundary spin is *disentangled* from the rest of the system. Thus the apparent paradox between the stroboscopic dynamics of the edge spin and the ergodic properties of the Floquet eigenstates gets resolved in the thermodynamic limit making the phenomenon truly athermal.

Interestingly, we do find athermal entanglement signatures also in the finite size Floquet eigenstates when every fourth site is driven and the system is bipartitioned into driven and undriven sites [see Fig. 10(e)]. For many eigenstates, the entanglement remains close to $\ln 2$, as can be seen in Fig. 10(d). Note that typical states in general should satisfy volume-law scaling for such bipartitions, an example being the protocol $s_d = \{1\}$ as shown in Fig. 10(c). Therefore our most efficient protocol ($s_d = \{1, 5, 9, 13\}$) generates exponentially many Floquet eigenstates with *subextensive* (athermal) entanglement, for a bipartition separating the driven and undriven sites. However, any random bipartition such as half-chain entanglement appears to produce a volume law scaling which is reminiscent of the behavior of rainbow states [104,105]. Our entanglement results showcase a rich and complex structure based on the geometry of the partitioning, where we observe signatures of both prethermal and athermal behaviors.

VI. CONCLUSION AND DISCUSSION

The phenomena of SZM where a quasilocal conservation law localized on the boundary, is proven to exist in one-dimensional integrable models with a discrete symmetry. In nonintegrable models, this operator usually develops a finite lifetime and ceases to be a conserved quantity in the thermodynamic limit. In this paper, we have shown the emergence of SZM in a nonintegrable spin chain through local Floquet engineering. We begin with a time-independent nonintegrable Hamiltonian with a continuous $U(1)$ symmetry which is broken by the periodic drive. We consider two classes of protocol, one where only the boundary spin is driven while the multisite drive also includes a subset of spins in the bulk. Through a second-order F-M expansion of the Floquet Hamiltonian, we show that the edge spin can undergo a significant slowdown for the boundary drive at certain freezing frequencies, which arise due to the nonlocal corrections in the Floquet Hamiltonian. In contrast, such higher-order processes were previously reported to destroy the dynamic localization in interacting systems [106]. At the freezing frequency, we argue that the system develops an approximate global discrete \mathbb{Z}_2 symmetry which is responsible for the boundary slowdown because of the formation of an approximate SZM. We find the boundary relaxation slows down with increasing system size but the relaxation time scale does not appear to grow exponentially.

We propose a multi-site drive protocol that further slows down the boundary relaxation. A special sequence of driven sites leads to the slowdown which scales exponentially with the number of driven sites. The emergence of a SZM is shown through signatures in spectral properties and eigenstate overlaps. The significantly enhanced slowdown of the boundary spin coexists with the rapid thermalization of the bulk degrees of freedom which realizes a novel regime that exhibits both thermal and athermal behavior. The intermediate athermal behavior also leaves an imprint in the entanglement structure of the Floquet eigenstates. Although the dynamics of the boundary spin relaxes on a time scale exponentially large in system size, the entanglement of the boundary spin is maximal in the Floquet eigenstates. Along with maximal single-site entanglement, random bipartitions also exhibit volume law scaling. Perhaps not surprisingly the bipartition involving the driven sites is significantly athermal. We leave the complete description of the entanglement structure as an interesting future problem. Expectation values of local observables in the Floquet eigenstates also exhibit hybrid thermal and athermal behavior reflecting the nontrivial consequences on the thermalization of the driven system. Our description provides a novel realization of an emergent SZM in a nonintegrable system realized through local Floquet engineering.

The stability of local athermal dynamics on a background of a thermalizing environment is of relevance for protecting quantum information. The emergence of quasilocal conservation laws with exponentially long relaxation times could potentially play a role near the many-body localization transition [107,108]. The interplay between the local Floquet drive and emergent symmetries can provide a path towards realizing novel states with a rich entanglement structure far from the ground state. A general understanding of the entanglement structure of states which are generically volume-law

entangled, yet contain elements of athermal character are potentially important for stabilizing nonequilibrium quantum orders away from the ground state. Our prescription for realizing local athermal dynamics utilizes the nonlocal multi-spin interactions generated by local Floquet engineering. This can be a valuable tool for engineering models with novel athermal character including QMBS [37]. We note that measurement of entanglement [92–94] in quantum simulation, preparation and characterization of genuinely entangled states [109] are within reach. The use of optical tweezers to hold the individual Rydberg atom opens the opportunity for implementing local drives (using an additional spatial laser pattern which addresses an arbitrary subset of atoms [110]) where the physics of SZM can be investigated [18,111]. Majorana zero modes in the ground state have been studied experimentally on solid state platforms [3,112,113]. Floquet driving provides another means of preparing such zero modes which can be robust to noise [114]. Recently, a periodically driven XXZ model has been implemented in a 24-qubit quantum simulator [115] and was found to host long-lived bound states even away from integrability [116]. Our model and protocol can also be implemented in the same setup with feasible modifications.

All relevant data present in this publication can be accessed at Ref. [117].

ACKNOWLEDGMENTS

We thank P. Sharma for collaboration on previous work. We thank D. Bluvstein, S. Li, J. Feldmeier, N. U. Koçluoğlu, and N. Maskara for discussion on the feasibility of implementing local drive in Rydberg atom experiments. R.M. and H.J.C. acknowledge support from Grant No. NSF DMR-2046570 and Florida State University (FSU) and the National High Magnetic Field Laboratory. The National High Magnetic Field Laboratory is supported by the National Science Foundation through Grant No. DMR-1644779 and by the state of Florida. A.P., B.M., and M.S. were funded by the European Research Council (ERC) under the European Union's Horizon 2020 research and innovation programme (Grant Agreement No. 853368). We also thank the Planck cluster and the Research Computing Center (RCC) at FSU for computing resources. The authors acknowledge the use of the UCL Myriad High Performance Computing Facility (Myriad@UCL), and associated support services, in the completion of this work.

APPENDIX A: CALCULATION OF THE FLOQUET HAMILTONIAN FOR SINGLE (EDGE) SITE DRIVING

Here we calculate the Floquet Hamiltonian H_F for a boundary-driven protocol, where a single site at the edge is driven. We first define the Hamiltonian and the drive protocol

$$H(t) = H_0 + f(t)V, \quad (\text{A1})$$

where $H_0 = \sum_{i=1}^{N-1} (-1)^i \mathbf{S}_i \cdot \mathbf{S}_{i+1} - h \sum_{i=1}^N S_i^z$, $f(t) = \gamma \text{sgn}(\sin(\omega t))$, and $V = S_1^x$, and we are using open boundary conditions.

We first apply a rotating-wave transformation to the time-dependent Hamiltonian,

$$H_{\text{rot}}(t) = W^\dagger H(t)W - iW^\dagger \partial_t W, \quad (\text{A2})$$

where

$$W(t) = e^{-i \int_0^t dt' f(t')V} = e^{-i\theta(t)S_1^x}, \quad (\text{A3})$$

with $\theta(t) = \gamma t \sum_n [\Theta(n\tau + \tau/2 - t) \Theta(t - n\tau)] + \gamma(\tau - t) \sum_n [\Theta((n+1)\tau - t) \Theta(t - (n\tau + \tau/2))]$, where Θ is a Heaviside step function. Firstly, this eliminates the explicit presence of the driving term in the time-dependent Hamiltonian, and secondly, H_F obtained in this way yields a resummed expression in ω (which increases the radius of convergence of the series) and can be considered as a perturbative expansion in $1/\gamma$ only. This allows us to consider all possible ω but restrict ourselves to a high drive amplitude regime. We obtain

$$\begin{aligned} H_{\text{rot}}(t) &= W^\dagger H_0 W \\ &= -S_1^x S_2^x - \cos \theta (S_1^y S_2^y + S_1^z S_2^z) \\ &\quad + \sin \theta (S_1^z S_2^y - S_1^y S_2^z) - h (\cos \theta S_1^z + \sin \theta S_1^y) \\ &\quad + \sum_{i=2}^{N-1} (-1)^i \mathbf{S}_i \cdot \mathbf{S}_{i+1} - h \sum_{i=2}^N S_i^z, \end{aligned} \quad (\text{A4})$$

where we have used $W^\dagger S_1^z W = \cos(\theta)S_1^z + \sin(\theta)S_1^y$ and $W^\dagger S_1^y W = -\sin(\theta)S_1^z + \cos(\theta)S_1^y$. For brevity, we replace $\theta(t)$ by θ .

The stroboscopic Floquet Hamiltonian in the F-M expansion is given by

$$H_F = \sum_{l=0}^{\infty} H_F^{(l)}. \quad (\text{A5})$$

We calculate this expression analytically up to the second term ($l=2$) in the sections below.

1. $l=0$ term in F-M

The $l=0$ Floquet Hamiltonian is just the time-averaged $H_{\text{rot}}(t)$ over one time period,

$$\begin{aligned} H_F^{(0)} &= \frac{1}{\tau} \int_0^\tau H_{\text{rot}}(t) dt \\ &= -S_1^x S_2^x - \frac{h}{\lambda} [\sin(\lambda)S_1^z + (1 - \cos \lambda)S_1^y] \\ &\quad - \frac{\sin \lambda}{\lambda} (S_1^y S_2^y + S_1^z S_2^z) + \frac{1 - \cos \lambda}{\lambda} (S_1^z S_2^y - S_1^y S_2^z) \\ &\quad + \sum_{i=2}^{N-1} (-1)^i \mathbf{S}_i \cdot \mathbf{S}_{i+1} - h \sum_{i=2}^N S_i^z. \end{aligned} \quad (\text{A6})$$

We have used the following integrals: $I_1[\cos \theta] = 2 \sin(\lambda)/\gamma$, $I_1[\sin \theta] = 2(1 - \cos \lambda)/\gamma$, where $I_1[x] \equiv \int_0^\tau x dt$ and $\lambda = \gamma\tau/2$. The form of this Hamiltonian suggests that if we choose the drive parameters accordingly ($\gamma\tau = 4k\pi$) then S_1^x is stroboscopically conserved, as $[S_1^x, H_F^{(0)}] = 0$ in this case.

2. $l = 1$ term in F-M

The first term in F-M is given by

$$H_F^{(1)} = \frac{1}{2!i\tau} \int_0^\tau dt_1 \int_0^{t_1} dt_2 [H_{\text{rot}}(t_1), H_{\text{rot}}(t_2)]. \quad (\text{A7})$$

We obtain

$$\begin{aligned} & [H_{\text{rot}}(t_1), H_{\text{rot}}(t_2)] \\ &= is_{12} \{ S_1^x (2h^2 + 4hS_2^z + 1)c_{12} - 2S_1^y [2hS_2^x s_{12} \\ &\quad - S_2^x S_3^y c_{12} - S_2^x S_3^z s_{12} + S_3^x S_2^y c_{12} + S_3^x S_2^z s_{12}] \\ &\quad - 2S_1^z [2hS_2^x c_{12} + S_2^x S_3^y s_{12} - S_2^x S_3^z c_{12} - S_3^x S_2^y s_{12} \\ &\quad + S_3^x S_2^z c_{12}] - S_2^x c_{12} \}, \end{aligned} \quad (\text{A8})$$

where we denote $\theta(t_1) = \theta_1$, $\theta(t_2) = \theta_2$, and use a short-hand notation $s_{12} \equiv \sin[(\theta_1 - \theta_2)/2]$ and $c_{12} \equiv \cos[(\theta_1 - \theta_2)/2]$. By performing the integrals, we find

$$H_F^{(1)} = 0. \quad (\text{A9})$$

Here we have used $I_2[\sin(\theta_1 - \theta_2)] = 0$, $I_2[\cos \theta_1] = I_2[\cos \theta_2] = \tau \sin(\lambda)/\gamma$, $I_2[\sin \theta_1] = I_2[\sin \theta_2] = \tau(1 - \cos \lambda)/\gamma$ where $I_2[x] = \int_0^\tau dt_1 \int_0^{t_1} dt_2 x$. Thus we find that the first term in F-M is zero.

3. $l = 2$ term in F-M

The second term in F-M is given by

$$\begin{aligned} H_F^{(2)} &= \frac{1}{3!\tau^2} \int_0^\tau dt_1 \int_0^{t_1} dt_2 \int_0^{t_2} dt_3 \\ &\times ([H_{\text{rot}}(t_1), [H_{\text{rot}}(t_2), H_{\text{rot}}(t_3)]] + (1 \leftrightarrow 3)). \end{aligned} \quad (\text{A10})$$

Calculation of these higher-order nested commutators is straightforward but unwieldy. In this section, we will consider only the renormalization of $H_F^{(0)}$, i.e., only the one- and the two-site terms which involve spin operators at the driven (boundary) site, more specifically only S_1^y and S_1^z which does not commute with S_1^x . We designate this part $H_{F, \text{loc}}^{(2)}$, and show that even the $\mathcal{O}(1/\gamma)$ terms present in it is sufficient to demonstrate the absence of dynamic freezing of the edge spin. Later we will also consider the other terms which are mostly long-range in nature ($H_{F, \text{nonloc}}^{(2)}$) and responsible for the enhanced freezing of the boundary spin. So, $H_F^{(2)} = H_{F, \text{loc}}^{(2)} + H_{F, \text{nonloc}}^{(2)}$.

Now, we have

$$\begin{aligned} & \{[H_{\text{rot}}(t_1), [H_{\text{rot}}(t_2), H_{\text{rot}}(t_3)]] + (1 \leftrightarrow 3)\}_{\text{loc}} \\ &= A_1(\boldsymbol{\theta})S_1^z + A_2(\boldsymbol{\theta})S_1^y + A_3(\boldsymbol{\theta})S_1^x S_2^z + A_4(\boldsymbol{\theta})S_1^y S_2^y \\ &\quad + A_5(\boldsymbol{\theta})S_1^z S_2^y + A_6(\boldsymbol{\theta})S_1^y S_2^z + \dots, \end{aligned} \quad (\text{A11})$$

where $\boldsymbol{\theta} \equiv (\theta_1, \theta_2, \theta_3)$. As one can see, these terms are exactly the same as appearing in the $l = 0$ term, thus only renormalizing their strength.

The coefficients are

$$\begin{aligned} A_1(\boldsymbol{\theta}) &= -\frac{h}{2} [c_1 + c_3 - 2c_2 + 2(1 + h^2)(s_1 s_2 c_3 + c_1 s_2 s_3 \\ &\quad - 2s_1 c_2 s_3)], \end{aligned} \quad (\text{A12})$$

$$\begin{aligned} A_2(\boldsymbol{\theta}) &= -\frac{h}{2} [s_1 + s_3 - 2s_2 + 2(1 + h^2)(s_1 c_2 c_3 + c_1 c_2 s_3 \\ &\quad - 2c_1 s_2 c_3)], \end{aligned} \quad (\text{A13})$$

$$\begin{aligned} A_3(\boldsymbol{\theta}) &= -\frac{1}{2} [c_1 + c_3 - 2c_2 + 2(1 + 3h^2)(s_1 s_2 c_3 + c_1 s_2 s_3 \\ &\quad - 2s_1 c_2 s_3)], \end{aligned} \quad (\text{A14})$$

$$\begin{aligned} A_4(\boldsymbol{\theta}) &= -\frac{1}{2} [(1 + 4h^2)(c_1 + c_3 - 2c_2) \\ &\quad + 2(1 + h^2)(s_1 s_2 c_3 + c_1 s_2 s_3 - 2s_1 c_2 s_3)], \end{aligned} \quad (\text{A15})$$

$$\begin{aligned} A_5(\boldsymbol{\theta}) &= \frac{1}{2} [(1 + 4h^2)(s_1 + s_3 - 2s_2) \\ &\quad + 2(1 + h^2)(s_1 c_2 c_3 + c_1 c_2 s_3 - 2c_1 s_2 c_3)], \end{aligned} \quad (\text{A16})$$

$$\begin{aligned} A_6(\boldsymbol{\theta}) &= -\frac{1}{2} [s_1 + s_3 - 2s_2 + 2(1 + 3h^2)(s_1 c_2 c_3 \\ &\quad + c_1 c_2 s_3 - 2c_1 s_2 c_3)], \end{aligned} \quad (\text{A17})$$

where we use a short-hand notation $s_i \equiv \sin \theta_i$, $c_i \equiv \cos \theta_i$. This yields the following integrals ($I_3[x] \equiv \int_0^\tau dt_1 \int_0^{t_1} dt_2 \int_0^{t_2} dt_3 x$):

$$I_3[A_1(\boldsymbol{\theta})] = \frac{12h\gamma\tau(h^2 + 1)\cos\lambda + h(\tau^2\gamma^2 - 8h^2 + 16)\sin\lambda}{4\gamma^3} - \frac{8h(h^2 + 1)\sin 2\lambda + 12h\gamma\tau}{4\gamma^3}, \quad (\text{A18})$$

$$I_3[A_2(\boldsymbol{\theta})] = \frac{8h(2h^2 - 1)\cos\lambda + 8h(h^2 + 1)\cos 2\lambda - 24h^3}{4\gamma^3} + \frac{12h\gamma\tau(h^2 + 1)\sin\lambda - h\gamma^2\tau^2(\cos\lambda + 2)}{4\gamma^3}, \quad (\text{A19})$$

$$I_3[A_3(\boldsymbol{\theta})] = \frac{(-24h^2 + \tau^2\gamma^2 + 16)\sin\lambda - 8(3h^2 + 1)\sin 2\lambda}{4\gamma^3} + \frac{12(3h^2 + 1)\gamma\tau\cos\lambda - 12\gamma\tau}{4\gamma^3}, \quad (\text{A20})$$

$$I_3[A_4(\boldsymbol{\theta})] = \frac{[(4h^2 + 1)\tau^2\gamma^2 + 88h^2 + 16]\sin\lambda + 12(h^2 + 1)\gamma\tau\cos\lambda}{4\gamma^3} - \frac{12(4h^2 + 1)\gamma\tau + 8(h^2 + 1)\sin 2\lambda}{4\gamma^3}, \quad (\text{A21})$$

$$I_3[A_5(\boldsymbol{\theta})] = \frac{8(10h^2 + 1)\cos\lambda - 8(h^2 + 1)\cos 2\lambda - 72h^2}{4\gamma^3} + \frac{(4h^2 + 1)\gamma^2\tau^2(\cos\lambda + 2) - 12\gamma\tau(h^2 + 1)\sin\lambda}{4\gamma^3}, \quad (\text{A22})$$

$$I_3[A_6(\boldsymbol{\theta})] = \frac{12\gamma\tau(3h^2 + 1)\sin\lambda - \gamma^2\tau^2(\cos\lambda + 2)}{4\gamma^3} - \frac{16\sin^2(\frac{\lambda}{2})[2(3h^2 + 1)\cos\lambda + 12h^2 + 1]}{4\gamma^3}, \quad (\text{A23})$$

TABLE I. Analytical expressions of the matrix element $H_F(2, 1)$ from F-M expansion.

	$H_F^{(0)} + H_F^{(1)} + H_{F,\text{loc}}^{(2)}[\mathcal{O}(\frac{1}{\gamma})]$	$H_F^{(0)} + H_F^{(1)} + H_{F,\text{loc}}^{(2)}[\mathcal{O}(\frac{1}{\gamma^3})]$
$\text{Re}[H_F(2, 1)]$	$-\frac{h \sin \lambda}{\gamma \tau} \left(1 + \frac{\tau^2}{48}\right)$	$\frac{8(h+h^3) \sin 2\lambda + 12h\gamma\tau - 12\gamma\tau(h+h^3) \cos \lambda + h \sin \lambda [8(h^2-2) - (\tau^2+48)\gamma^2]}{48\tau\gamma^3}$
$\text{Im}[H_F(2, 1)]$	$-\frac{h}{\gamma\tau}(1 - \cos \lambda) + \frac{h\tau(2+\cos \lambda)}{48\gamma}$	$\frac{24h^3+2h\gamma^2(\tau^2-24)-8(h+h^3) \cos 2\lambda-12\gamma\tau(h+h^3) \sin \lambda+h \cos \lambda [8-16h^2+(\tau^2+48)\gamma^2]}{48\tau\gamma^3}$

where we have used the values of the integrals,

$$I_3[c_1] = I_3[c_3] = \frac{1}{4\gamma^3} [4\gamma\tau + (\sin \lambda)(\gamma^2\tau^2 - 8)], \quad I_3[c_2] = \frac{1}{2\gamma^3} [-4\gamma\tau + (\sin \lambda)(\gamma^2\tau^2 + 8)],$$

$$I_3[s_1] = I_3[s_3] = \frac{1}{4\gamma^3} [2\gamma^2\tau^2 - (\cos \lambda)(\gamma^2\tau^2 - 8) - 8], \quad I_3[s_2] = \frac{1}{2\gamma^3} \left[8 \sin^2 \frac{\lambda}{2} - (\cos \lambda)(\gamma^2\tau^2 + 4) + 4 \right], \quad (\text{A24})$$

and

$$I_3[s_1c_2c_3] = \frac{10 - 6 \cos \lambda - 6 \cos 2\lambda + 2 \cos 3\lambda - 6\lambda \sin \lambda}{6\gamma^3}, \quad I_3[c_1s_2c_3] = \frac{-4 + 3 \cos \lambda + \cos 3\lambda + 6\lambda \sin \lambda}{3\gamma^3},$$

$$I_3[c_1c_2s_3] = \frac{10 - 6 \cos \lambda - 6 \cos 2\lambda + 2 \cos 3\lambda - 6\lambda \sin \lambda}{6\gamma^3}, \quad I_3[s_1c_2s_3] = \frac{3 \sin \lambda - 6 \sin 2\lambda + \sin 3\lambda + 6\lambda \cos \lambda}{3\gamma^3},$$

$$I_3[s_1s_2c_3] = \frac{12 \sin \lambda - 6 \sin 2\lambda + 2 \sin 3\lambda - 6\lambda \cos \lambda}{6\gamma^3}, \quad I_3[c_1s_2s_3] = \frac{12 \sin \lambda - 6 \sin 2\lambda + 2 \sin 3\lambda - 6\lambda \cos \lambda}{6\gamma^3}. \quad (\text{A25})$$

Values of these integrals substituted in Eq. (A10) directly give the $H_{F,\text{loc}}^{(2)}$. The interesting fact is that even $H_{F,\text{loc}}^{(2)}$ contains terms which are $\mathcal{O}(1/\gamma)$. This modifies the freezing conditions which were believed to be true at least in $\mathcal{O}(1/\gamma)$.

4. Full H_F (local)

As mentioned before, the resummed H_F is a series expansion in $1/\gamma$ and for many purposes, we can neglect the higher order (which are at least $1/\gamma^2$ or smaller) terms. Therefore, summing up all the one and two site terms up to the second order in F-M expansion which are $\mathcal{O}(1/\gamma)$, we get the local Floquet effective Hamiltonian [Eq. (18) in the main text]

$$H_{F,\text{loc}} \left[\mathcal{O} \left(\frac{1}{\gamma} \right) \right] = H_F^{(0)} + H_F^{(1)} + H_{F,\text{loc}}^{(2)} [\mathcal{O}(1/\gamma)] + \dots$$

$$= -S_1^x S_2^x - \frac{2 \sin \lambda}{\gamma \tau} \left[\left(1 + \frac{(1+4h^2)\tau^2}{48} \right) S_1^y S_2^y + \left(1 + \frac{\tau^2}{48} \right) S_1^z S_2^z \right]$$

$$+ \frac{2}{\gamma \tau} \left[\left(1 - \cos \lambda - \frac{(1+4h^2)\tau^2(2+\cos \lambda)}{48} \right) S_1^z S_2^y - \left(1 - \cos \lambda - \frac{\tau^2(2+\cos \lambda)}{48} \right) S_1^y S_2^z \right]$$

$$- \frac{2h}{\gamma \tau} \left[(\sin \lambda) \left(1 + \frac{\tau^2}{48} \right) S_1^z + \left(1 - \cos \lambda - \frac{\tau^2(2+\cos \lambda)}{48} \right) S_1^y \right] + \sum_{i=2}^{N-1} (-1)^i \mathbf{S}_i \cdot \mathbf{S}_{i+1} - h \sum_{i=2}^N S_i^z. \quad (\text{A26})$$

For concreteness, we also write the full local H_F (considering the full contribution from the $l = 2$ term in F-M expansion)

$$H_{F,\text{loc}} \left[\mathcal{O} \left(\frac{1}{\gamma^3} \right) \right] = H_F^{(0)} + H_F^{(1)} + H_{F,\text{loc}}^{(2)} \left[\mathcal{O} \left(\frac{1}{\gamma^3} \right) \right]$$

$$= -S_1^x S_2^x - \left[\left(\frac{\sin \lambda}{\lambda} - a_4(\mathbf{p}) \right) S_1^y S_2^y + \left(\frac{\sin \lambda}{\lambda} - a_3(\mathbf{p}) \right) S_1^z S_2^z \right] + \left[\left(\frac{1 - \cos \lambda}{\lambda} + a_5(\mathbf{p}) \right) S_1^z S_2^y \right.$$

$$\left. - \left(\frac{1 - \cos \lambda}{\lambda} - a_6(\mathbf{p}) \right) S_1^y S_2^z \right] - \left[\left(\frac{h \sin \lambda}{\lambda} - a_1(\mathbf{p}) \right) S_1^z + \left(\frac{h(1 - \cos \lambda)}{\lambda} - a_2(\mathbf{p}) \right) S_1^y \right]$$

$$+ \sum_{i=2}^{N-1} (-1)^i \mathbf{S}_i \cdot \mathbf{S}_{i+1} - h \sum_{i=2}^N S_i^z, \quad (\text{A27})$$

where $a_i(\mathbf{p}) = -I_3[A_i(\boldsymbol{\theta})]/(6\tau)$.

To demonstrate the accuracy of the resummed F-M expansion, we compute the matrix element $H_F(2, 1)$ using Eq. (A26), Eq. (A27) and summarize the con-

solidated expression in Table I. We compare these expressions with exact numerics in Fig. 4 in the main text.

5. Additional (long range) terms in $H_F^{(2)} : H_{F, \text{nonloc}}^{(2)}$

Here we consider additional terms in $H_F^{(2)}$ which are long-range (i.e., beyond nearest neighbor) and multispin in nature which enhances the freezing of the boundary site. These terms are expected to be perturbatively suppressed for global driving, keeping the quasiloc nature of H_F intact. Here, we will show that for local driving these terms can be similar in strength to the zeroth order terms.

$$\begin{aligned}
& \{[H_{\text{rot}}(t_1), [H_{\text{rot}}(t_2), H_{\text{rot}}(t_3)]] + (1 \leftrightarrow 3)\}_{\text{nonloc}} \\
&= \beta(\boldsymbol{\theta})(3S_1^z S_3^z + 4S_1^z S_2^y S_3^z S_4^y - 4S_1^z S_2^y S_3^z S_4^y \\
&\quad - 4S_1^z S_2^x S_3^z S_4^x + 4S_1^z S_2^x S_3^z S_4^x + 3S_1^y S_3^y \\
&\quad + 12hS_1^y S_2^y S_3^z S_4^y - 4S_1^y S_2^z S_3^z S_4^y - 12hS_1^y S_2^z S_3^z S_4^y \\
&\quad - 4S_1^y S_2^z S_3^z S_4^z - 4S_1^y S_2^x S_3^z S_4^x + 4S_1^y S_2^x S_3^z S_4^y) \\
&\quad + \eta(\boldsymbol{\theta})(3S_1^z S_3^y - 12hS_1^z S_2^y S_3^z - 4S_1^z S_2^z S_3^z S_4^y \\
&\quad + 12hS_1^z S_2^z S_3^y + 4S_1^z S_2^z S_3^z S_4^z + 4S_1^z S_2^x S_3^z S_4^x \\
&\quad - 4S_1^z S_2^x S_3^z S_4^y + 3S_1^y S_3^z + 4S_1^y S_2^y S_3^z S_4^z \\
&\quad + 4S_1^y S_2^z S_3^z S_4^y + 4S_1^y S_2^x S_3^z S_4^x - 4S_1^y S_2^x S_3^z S_4^z) + \dots, \tag{A28}
\end{aligned}$$

where the “...” represents some terms which commute with S_1^x . The coefficients and their integrals are given by

$$\begin{aligned}
\beta(\boldsymbol{\theta}) &= \frac{1}{4}[\cos \theta_1 + \cos \theta_3 - 2 \cos \theta_2], \\
I_3[\beta(\boldsymbol{\theta})] &= \frac{12\tau\gamma - (\tau^2\gamma^2 + 24) \sin \lambda}{8\gamma^3}, \\
\eta(\boldsymbol{\theta}) &= \frac{1}{4}[\sin \theta_1 + \sin \theta_3 - 2 \sin \theta_2], \\
I_3[\eta(\boldsymbol{\theta})] &= \frac{\tau^2\gamma^2(\cos \lambda + 2) - 48 \sin^2 \frac{\lambda}{2}}{8\gamma^3}. \tag{A29}
\end{aligned}$$

Substituting Eq. (A28) and the values of the integrals in Eq. (A29) to Eq. (A10), we directly get the nonlocal part of $H_F^{(2)}$. The crucial thing to note here is that, even at the special frequencies ($\gamma\tau = 4n\pi$), some of the integrals in Eq. (A29) (which determines the strength of the long-range terms) are not only nonzero, but similar in magnitude to the zeroth order terms, i.e., $\mathcal{O}(1/\gamma)$. Counterintuitively, as shown in the main text, these terms take part in enhancing the freezing of the boundary spin at ω_m^k .

APPENDIX B: CALCULATION OF H_F FOR TWO-SITE DRIVING

Here we give a detailed derivation of the Floquet Hamiltonian for two-site driving, i.e., when a second site (say, site j)

is driven in addition to the boundary site (site 1) following the same drive protocol. The time-dependent part of the Hamiltonian is $\gamma \text{sgn}(\sin(\omega t))(S_1^x + S_j^x)$ and we follow the same prescription of calculating H_F as charted out in the previous section for single site driving. The rotating wave transformation is generated by the operator: $W(t) = e^{-i\theta(t)(S_1^x + S_j^x)}$ which gives for $j > 2$

$$\begin{aligned}
H_{\text{rot}}^{j>2}(t) &= W^\dagger H_0 W \\
&= -S_1^x S_2^x - \cos \theta (S_1^y S_2^y + S_1^z S_2^z) + \sin \theta (S_1^z S_2^y - S_1^y S_2^z) \\
&\quad + (-1)^{j-1} [S_{j-1}^x S_j^x + \cos \theta (S_{j-1}^y S_j^y + S_{j-1}^z S_j^z) \\
&\quad - \sin \theta (S_{j-1}^z S_j^y - S_{j-1}^y S_j^z)] \\
&\quad + (-1)^j [S_j^x S_{j+1}^x + \cos \theta (S_j^y S_{j+1}^y + S_j^z S_{j+1}^z) \\
&\quad - \sin \theta (S_j^z S_{j+1}^y - S_j^y S_{j+1}^z)] \\
&\quad - h [\cos \theta (S_1^z + S_j^z) + \sin \theta (S_1^y + S_j^y)] \\
&\quad + \sum_{i=2}^{j-2} (-1)^i \mathbf{S}_i \cdot \mathbf{S}_{i+1} + \sum_{i=j+1}^{N-1} (-1)^i \mathbf{S}_i \cdot \mathbf{S}_{i+1} \\
&\quad - h \left(\sum_{i=2}^{j-1} S_i^z + \sum_{i=j+1}^N S_i^z \right), \tag{B1}
\end{aligned}$$

and for $j = 2$

$$\begin{aligned}
H_{\text{rot}}^{j=2}(t) &= W^\dagger H_0 W \\
&= -\mathbf{S}_1 \cdot \mathbf{S}_2 + S_2^x S_3^x \\
&\quad + \cos \theta (S_2^y S_3^y + S_2^z S_3^z) - \sin \theta (S_2^z S_3^y - S_2^y S_3^z) \\
&\quad - h [\cos \theta (S_1^z + S_2^z) + \sin \theta (S_1^y + S_2^y)] \\
&\quad + \sum_{i=3}^{N-1} (-1)^i \mathbf{S}_i \cdot \mathbf{S}_{i+1} - h \sum_{i=3}^N S_i^z. \tag{B2}
\end{aligned}$$

Note that SU(2) symmetry is locally restored for the $j = 2$ case as the interaction term $\mathbf{S}_1 \cdot \mathbf{S}_2$ is fully rotationally invariant. This reduces the number of additional terms generated by the drive and leads to a significant suppression of the matrix element $H_F(4, 1)$ (where $|4\rangle = \sigma_1^z \sigma_2^z |1\rangle$) which in turn reduces the rate of relaxation of the spins at sites 1 and 2. We focus on calculating H_F for $s_d = \{1, 5\}$ in the rest of this Appendix.

Proceeding in the same manner as before, we get the $l = 0$ term in F-M,

$$\begin{aligned}
H_F^{(0)} &= \frac{1}{\tau} \int_0^\tau H_{\text{rot}}^{j=5}(t) dt = -S_1^x S_2^x - \frac{\sin \lambda}{\lambda} (S_1^y S_2^y + S_1^z S_2^z) + \frac{1 - \cos \lambda}{\lambda} (S_1^z S_2^y - S_1^y S_2^z) - \frac{h}{\lambda} [\sin \lambda S_1^z + (1 - \cos \lambda) S_1^y] \\
&\quad + S_4^x S_5^x + \frac{\sin \lambda}{\lambda} (S_4^y S_5^y + S_4^z S_5^z) - \frac{1 - \cos \lambda}{\lambda} (S_4^z S_5^y - S_4^y S_5^z) - \frac{h}{\lambda} [\sin \lambda S_5^z + (1 - \cos \lambda) S_5^y] \\
&\quad - S_3^x S_6^x - \frac{\sin \lambda}{\lambda} (S_5^y S_6^y + S_5^z S_6^z) + \frac{1 - \cos \lambda}{\lambda} (S_5^z S_6^y - S_5^y S_6^z)
\end{aligned}$$

$$+ \mathbf{S}_2 \cdot \mathbf{S}_3 - \mathbf{S}_3 \cdot \mathbf{S}_4 + \sum_{i=6}^{N-1} (-1)^i \mathbf{S}_i \cdot \mathbf{S}_{i+1} - h \left(S_2^z + S_3^z + S_4^z + \sum_{i=6}^N S_i^z \right). \quad (\text{B3})$$

We again find, $H_F^{(1)} = 0$.

We notice that all local terms (one and two-body operators) in $H_F^{(2)}$ involving the spin operators at site 1 (S_1^x, S_1^y, S_1^z) are the same as for the case of boundary driving ($s_d = \{1\}$) given in Eq. (A11)–(A26) which means they are not affected by the drive at site 5. We do not attempt to calculate the full $H_F^{(2)}$ in this case as we find that it is not sufficient to have good matching with exact numerical data even for very simple events like a single spin flip at site 5 from the state $|\psi_0\rangle$ determined by the matrix element $H_F(17, 1)$ ($|1\rangle = |\psi_0\rangle$ and $|17\rangle = \sigma_5^z |\psi_0\rangle$). To this end, we find the following terms in $H_F^{(2)}$ which contribute to $H_F(17, 1)$,

$$\begin{aligned} & \{ [H_{\text{rot}}^{j=5}(t_1), [H_{\text{rot}}^{j=5}(t_2), H_{\text{rot}}^{j=5}(t_3)]] + (1 \leftrightarrow 3) \}_{\text{local}} \\ & = \dots + A(\boldsymbol{\theta}) S_5^z + B(\boldsymbol{\theta}) S_4^x S_5^z S_6^x \\ & \quad + C(\boldsymbol{\theta}) S_5^y + D(\boldsymbol{\theta}) S_4^x S_5^y S_6^x + \dots, \end{aligned} \quad (\text{B4})$$

where the first “ \dots ” in right-hand side stands for the same terms as in Eq. (A11) and the last “ \dots ” represent additional terms generated due to the driving of site 5. Note that unlike the driven boundary site, three body interaction terms are also contributing to flip the spin at the driven site 5 in addition to the local field terms (S_5^z, S_5^y). The coefficients of the terms in Eq. (B4) are given by

$$\begin{aligned} A(\boldsymbol{\theta}) &= -\frac{h}{2} [2(c_1 + c_3 - 2c_2) \\ & \quad + (1 + 2h^2)(s_1 s_2 c_3 + c_1 s_2 s_3 - 2s_1 c_2 s_3)], \\ B(\boldsymbol{\theta}) &= 6h(c_1 + c_3 - 2c_2), \\ C(\boldsymbol{\theta}) &= -\frac{h}{2} [s_1 + s_3 - 2s_2 \\ & \quad + (1 + 2h^2)(s_1 c_2 c_3 + c_1 c_2 s_3 - 2c_1 s_2 c_3)], \\ D(\boldsymbol{\theta}) &= 2h(s_1 + s_3 - 2s_2), \end{aligned} \quad (\text{B5})$$

where we again used notation $s_i \equiv \sin \theta_i$ and $c_i \equiv \cos \theta_i$. The corresponding integrals are given by

$$\begin{aligned} I_3[A(\boldsymbol{\theta})] &= \frac{h(-4h^2 + \tau^2 \gamma^2 + 22) \sin \lambda - 12h\tau\gamma}{2\gamma^3} \\ & \quad + \frac{3(2h^3 + h)\tau\gamma \cos \lambda - 2h(2h^2 + 1) \sin(2\lambda)}{2\gamma^3}, \\ I_3[B(\boldsymbol{\theta})] &= \frac{3h[12\tau\gamma - (\tau^2 \gamma^2 + 24) \sin \lambda]}{\gamma^3}, \\ I_3[C(\boldsymbol{\theta})] &= \frac{\tau\gamma(6(2h^3 + h) \sin \lambda - h\tau\gamma(\cos \lambda + 2))}{4\gamma^3} \\ & \quad - \frac{16h \sin^2 \frac{\lambda}{2} [(2h^2 + 1) \cos \lambda + 4h^2 - 1]}{4\gamma^3}, \\ I_3[D(\boldsymbol{\theta})] &= \frac{h[\tau^2 \gamma^2 (\cos \lambda + 2) - 48 \sin^2 \frac{\lambda}{2}]}{\gamma^3}. \end{aligned} \quad (\text{B6})$$

We find that the new three-body terms improve the agreement with exact numerics in this case but they are not sufficient and one needs to go to higher order. We leave this as a future problem.

APPENDIX C: GLOBAL DRIVING

In this section, we demonstrate a distinguishing feature of the perturbative structure of H_F for local and global driving. The time-independent part (H_0) remains the same as before, we only make the driving part spatially uniform by choosing $V = \gamma \text{sgn}(\sin(\omega t)) \sum_{i=1}^N S_i^x$. The rotating-frame Hamiltonian is now given by

$$\begin{aligned} H_{\text{rot}}(t) &= W^\dagger H_0 W = \sum_{i=1}^{N-1} (-1)^i \mathbf{S}_i \cdot \mathbf{S}_{i+1} \\ & \quad - h \left(\cos \theta \sum_{i=1}^N S_i^z + \sin \theta \sum_{i=1}^N S_i^y \right). \end{aligned} \quad (\text{C1})$$

$W(t)$ gives a global rotation of all the terms about the x axis. Consequently, the Heisenberg part remains intact because of the SU(2) symmetry. The zeroth term ($l = 0$) in the F-M is given by

$$\begin{aligned} H_F^{(0)} &= \sum_{i=1}^{N-1} (-1)^i \mathbf{S}_i \cdot \mathbf{S}_{i+1} \\ & \quad - \frac{h}{\lambda} \left[\sin \lambda \sum_{i=1}^N S_i^z + (1 - \cos \lambda) \sum_{i=1}^N S_i^y \right], \end{aligned} \quad (\text{C2})$$

where $\lambda = \gamma\tau/2$. We get $H_F^{(1)} = 0$ as before.

To calculate the 2nd term ($l = 2$) in F-M, we find

$$\begin{aligned} & \{ [H_{\text{rot}}(t_1), [H_{\text{rot}}(t_2), H_{\text{rot}}(t_3)]] + (1 \leftrightarrow 3) \} \\ & = -h^3 \left[A(\boldsymbol{\theta}) \sum_{i=1}^N S_i^z + B(\boldsymbol{\theta}) \sum_{i=1}^N S_i^y \right], \end{aligned} \quad (\text{C3})$$

where

$$\begin{aligned} A(\boldsymbol{\theta}) &= \sin \theta_2 \sin(\theta_1 + \theta_3) - 2 \sin \theta_1 \cos \theta_2 \sin \theta_3, \\ B(\boldsymbol{\theta}) &= \cos \theta_2 \sin(\theta_1 + \theta_3) - 2 \cos \theta_1 \sin \theta_2 \cos \theta_3. \end{aligned} \quad (\text{C4})$$

Thus, using the integrals in Eq. (A25), we get

$$H_F^{(2)} = a(\mathbf{p}) \sum_{i=1}^N S_i^z + b(\mathbf{p}) \sum_{i=1}^N S_i^y, \quad (\text{C5})$$

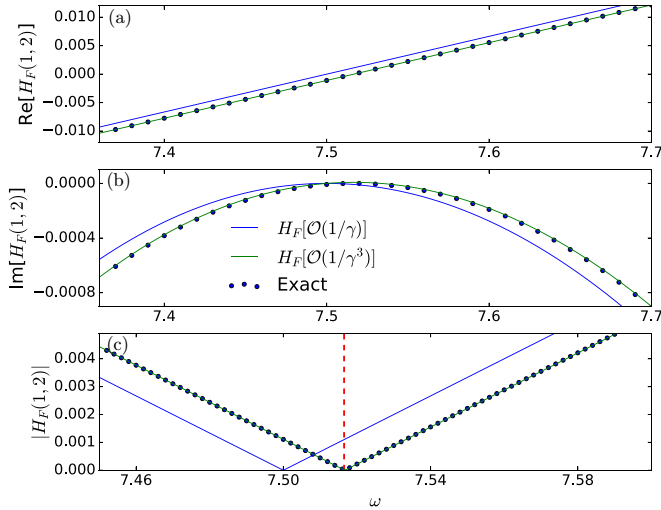


FIG. 11. The matrix element $H_F(2, 1)$ vs ω for global driving comparing $H_F^{(2)}$ with exact numerical data. $\gamma = 15$, $h = 1$, and $N = 8$.

where

$$a(\mathbf{p}) = \frac{h^3}{6\tau\gamma^3} [2(\sin \lambda + \sin 2\lambda) - 3\gamma\tau \cos \lambda],$$

$$b(\mathbf{p}) = \frac{h^3}{6\tau\gamma^3} [6 - 2(2 \cos \lambda + \cos 2\lambda) - 3\gamma\tau \sin \lambda]. \quad (\text{C6})$$

Note that, unlike the local driving, the $l = 2$ terms here are at least $\mathcal{O}(1/\gamma^2)$ or smaller. Finally, the full H_F can be obtained by adding all these contributions: $H_F[\mathcal{O}(1/\gamma^3)] = H_F^{(0)} + H_F^{(1)} + H_F^{(2)}$. Thus we see, only the field terms are renormalized but no additional interacting term is generated. Therefore, in this case, the global driving only induces a fully coherent oscillation from the initial x -polarized (ψ_0) state at any drive parameter regime. The driven state being a globally rotated version of ψ_0 always remains an eigenstate of the $SU(2)$ symmetric Heisenberg interaction part and hence does not suffer any dephasing. In this case, the field terms can get completely canceled at fine-tuned drive frequencies resulting in true freezing of the wave function. The exact numerical data including the shift of the freezing frequencies (from ω_c^k to ω_m^k) can be accurately captured by $H_F[\mathcal{O}(1/\gamma^3)]$ as shown in Fig. 11.

APPENDIX D: LEVEL STATISTICS OF THE FLOQUET HAMILTONIAN

In this Appendix, we study the level statistics of the Floquet Hamiltonian (H_F). At generic drive frequencies ($\omega \lesssim \gamma$) H_F hardly has any symmetry and hence we increasingly order the Floquet eigenvalues (ϵ_i) in the entire first Floquet BZ. At the freezing frequencies, D_z is an emergent conserved quantity and we confine ourselves in a specific D_z sector. We then calculate the gap between consecutive eigenvalues: $g_i = \epsilon_{i+1} - \epsilon_i$ (we are using a different symbol for the gap to distinguish it from the spectral gap defined in the main text)

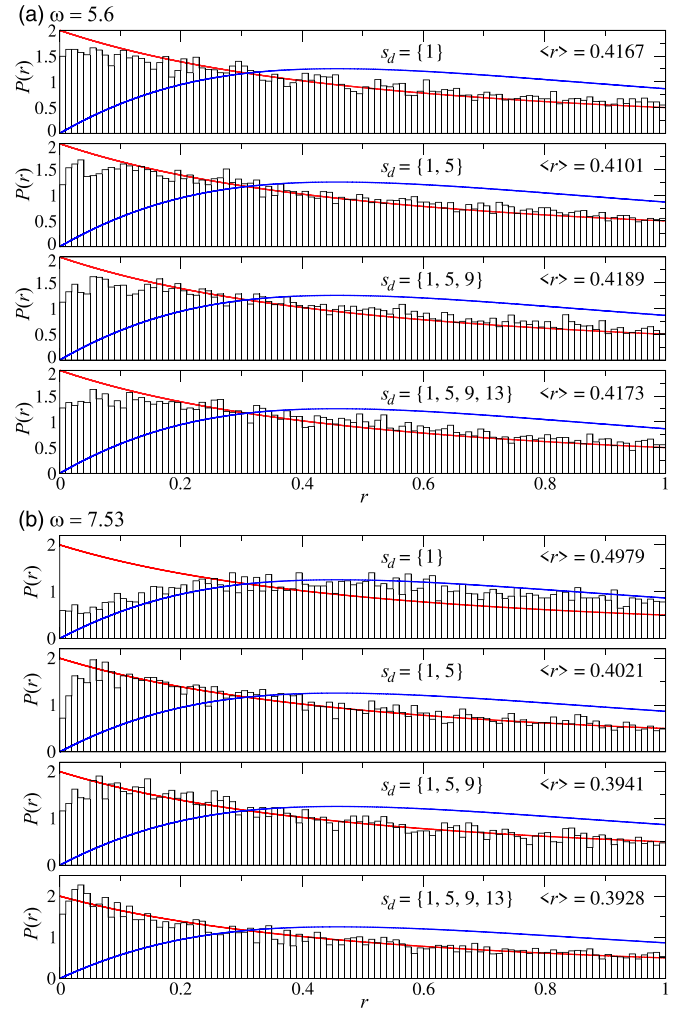


FIG. 12. Level statistics of the Floquet eigenvalues, (a) at a generic drive frequency $\omega = 5.6$ (b) at the freezing frequency $\omega = \omega_m^1 = 7.53$. The blue line corresponds to the Wigner surmise (an approximation to the GOE statistics of chaotic systems), while the red line is the Poisson distribution (integrable systems). $N = 14$, $\gamma = 15$.

and their ratios defined as

$$r_i = \frac{\min(g_i, g_{i+1})}{\max(g_i, g_{i+1})}. \quad (\text{D1})$$

The distribution of r_i gives important information about the integrability of the system. For example, chaotic (nonintegrable) systems exhibit a GOE distribution, whereas integrable systems admit Poisson level statistics. In our case, we find the distribution to be more like Poissonian at generic drive frequencies [see Fig. 12(a)]. Here we note that in addition to integrability (an unlikely possibility in our case), Poissonian statistics can appear in several other situations, for example, if there is some hidden unresolved symmetry or if the Hilbert space is fragmented. We find the following operator to be a good candidate of an approximate discrete symmetry at any frequency

$$\mathcal{M} = 2^N \prod_{i \in s_d} \left[\cos \frac{\lambda}{2} \left(S_i^z + \tan \frac{\lambda}{2} S_i^y \right) \right] \prod_{i \notin s_d} S_i^z, \quad (\text{D2})$$

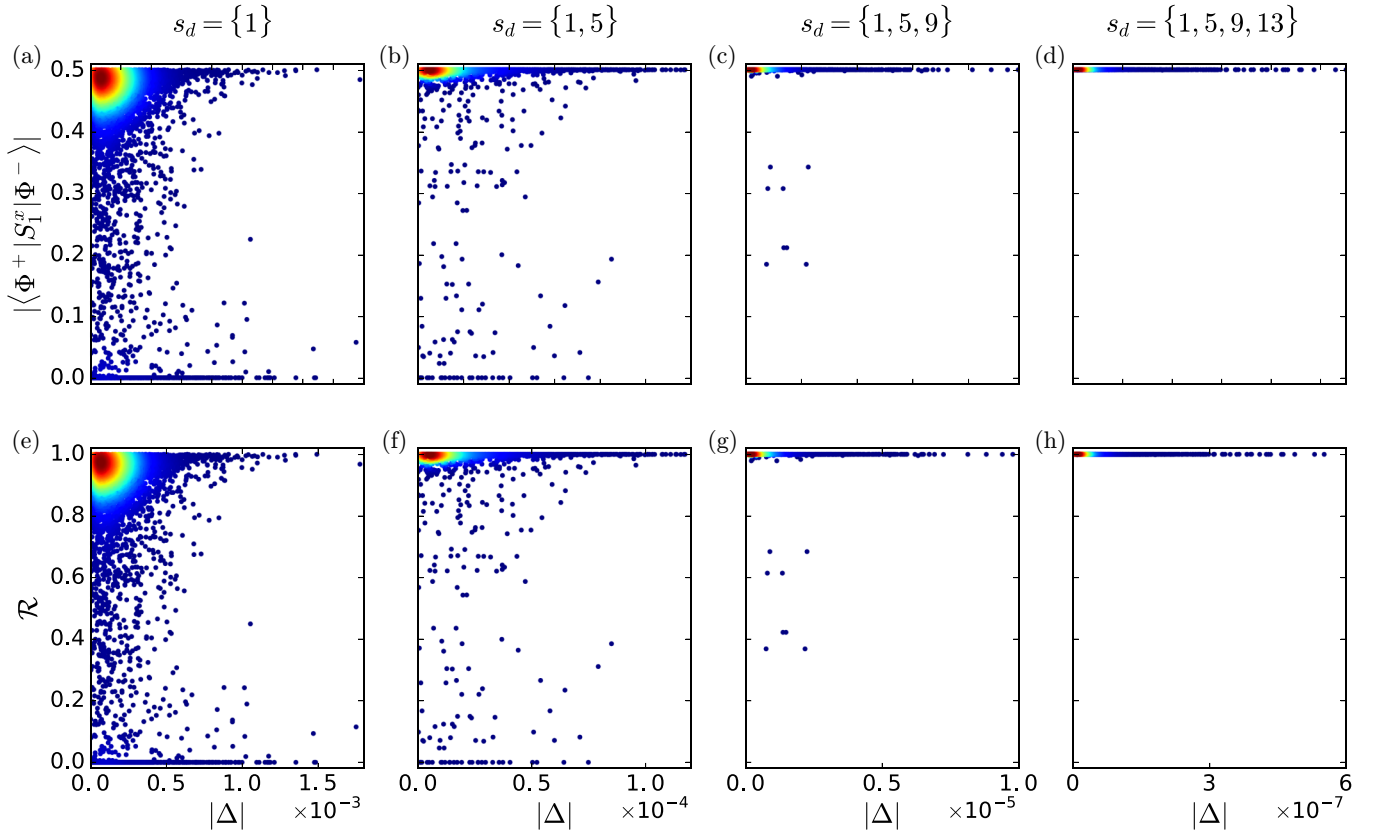


FIG. 13. The behavior of $|\langle \Phi^- | S_1^x | \Phi^+ \rangle|$ in the upper panels (a-d) in parallel with the behaviors of $\bar{\mathcal{R}}$ in the lower panels (e)-(h). The driven sites are mentioned on top of the upper panels (valid for both panels in each column). The values of $|\langle \Phi^- | S_1^x | \Phi^+ \rangle|$ are (a) 0.4275, (b) 0.4942, (c) 0.4996, (d) 0.4998 and the values of $\bar{\mathcal{R}}$ are (e) 0.8550, (f) 0.9883, (g) 0.9991, (h) 0.9996. $\gamma = 15$, $\omega = 7.53$, $N = 14$ for all the plots.

with eigenvalues ± 1 . In fact, \mathcal{M} is conserved exactly at the level of $H_F^{(0)}$ for $s_d = \{1\}$, i.e. $[\mathcal{M}, H_F^{(0)}] = 0$ for any λ . Note that \mathcal{M} converts to D_z when $\lambda = 2\pi k$. We also numerically find that for any driving protocol with every fourth site driven, $\langle \Phi_r | \mathcal{M} | \Phi_r \rangle \approx \pm 1$ on a broad range of λ . The existence of such operators, which may remain weakly conserved, is most likely the origin of the Poissonian nature of the level statistics at generic drive frequencies. At the freezing frequency, after resolving D_z , we find the distribution to resemble GOE for $s_d = \{1\}$ but again Poissonian for protocols $s_d = \{1, 5\}, \{1, 5, 9\}, \{1, 5, 9, 13\}$. This suggests that additional symmetries may emerge when increasing number of suitably chosen (every fourth) sites are driven with the freezing frequency.

APPENDIX E: MORE RESULTS ON THE EMERGENCE OF SZM AND ENTANGLEMENT OF THE FLOQUET EIGENSTATES

Here we corroborate the emergence of SZM (presented in the main text) with more numerical results. If a Floquet system described by the Floquet Hamiltonian H_F possesses a SZM with S_1^x as the leading part, then the whole Floquet spectrum can be decomposed into quasidegenerate eigenpairs $|\Phi_r^\pm\rangle$ (with $D^z |\Phi_r^\pm\rangle = \pm |\Phi_r^\pm\rangle$ and $H_F |\Phi_r^\pm\rangle = \epsilon_r^\pm |\Phi_r^\pm\rangle$) where $|\Phi_r^\pm\rangle$ can be obtained from $|\Phi_r^\mp\rangle$ under the action of S_1^x up to

a global phase. We increasingly order both ϵ_r^+ and ϵ_r^- s within the first Floquet-BZ. Such labeling of eigenpairs may lead to some subtleties in some cases which we clarify now. We find that some Floquet eigenpairs (say, ϵ_p^\pm), obtained in this way, may yield a super low value of $|\langle \Phi_p^- | S_1^x | \Phi_p^+ \rangle|$ instead of ~ 0.5 . Such ghost eigenpairs are found to appear always in pairs (say, $p, p+1$) and a cross pairing may restore the value of the matrix element i.e. $|\langle \Phi_{p(p+1)}^- | S_1^x | \Phi_{p+1(p)}^+ \rangle| \sim 0.5$. Such cross-pairing may also reduce one of the pairing gaps but then the other one will definitely increase. This kind of ghost pairs get rarer with the emergence of SZM. However, when one of the Floquet eigenvalues of a normal pair crosses the Floquet BZ boundary, that results in a cascade of mismatch between the increasingly ordered ϵ_r^\pm which generates ghost pairs throughout the spectrum. This leads to a sharp drop in $|\langle \Phi^- | S_1^x | \Phi^+ \rangle|$ at some ω which are mostly away from the special frequencies (ω_m^k) where even the conservation of D_z , the first criteria of having a SZM, does not satisfy. We discard such rare pathological points from our consideration while plotting Fig. 8(b) in the main text. Thus the correspondence between the increasingly ordered ϵ_r^\pm may get ill-defined at drive frequencies away from the slowest relaxation points (ω_m^k). But as we increase the number of optimally chosen driven sites (n_d^{th}) and tune the drive frequency towards ω_m , the correspondence gradually becomes more and more accurate signaling the emergence of SZM.

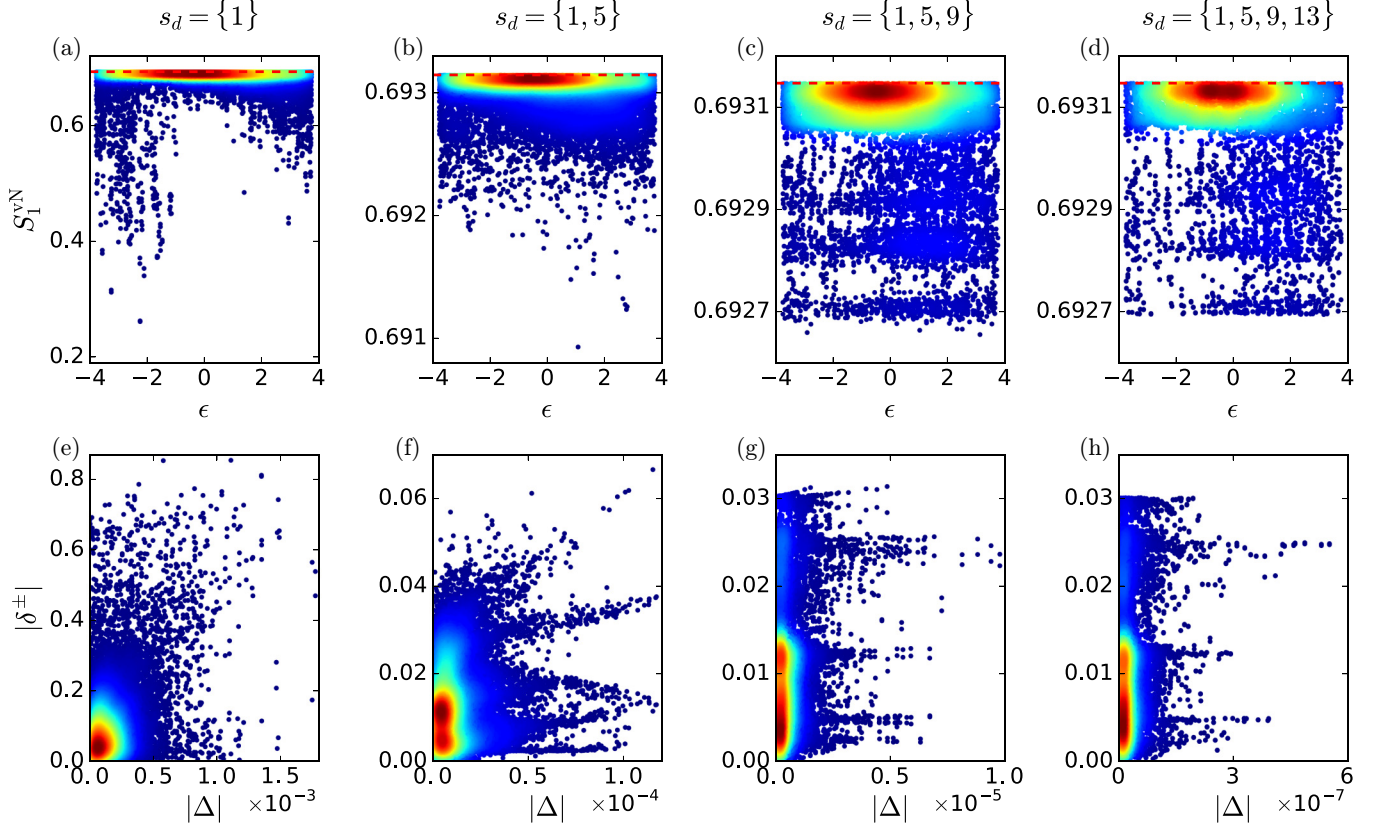


FIG. 14. The behavior of S_1^{vN} in all the Floquet eigenstates in the upper panels in parallel with the behavior of $|\delta^\pm|$ (not distinguished) in the lower panels. The average deviations of S_1^{vN} from the maximal value $\ln 2$ (shown in red dashed line) are (a) 1.21×10^{-2} , (b) 1.42×10^{-4} , (c) 8.89×10^{-5} , (d) 8.34×10^{-5} , and the average values of $|\delta^\pm|$ are (e) 0.11, (f) 1.38×10^{-2} , (g) 1.09×10^{-2} , and (h) 1.05×10^{-2} . All other parameters are the same as in Fig. 13.

We demonstrate this in Fig. 13 where we show the behavior of $|\langle \Phi_r^- | S_1^x | \Phi_r^+ \rangle|$ in parallel with the behaviors of \mathcal{R}_r (as defined in the main text) with increasing n_d^{th} . One can see that there are many pairs with $|\langle \Phi_r^- | S_1^x | \Phi_r^+ \rangle| < 0.5$ including the ghost pairs with $|\langle \Phi_r^- | S_1^x | \Phi_r^+ \rangle| \sim 0$ for $s_d = \{1\}$. The number of such pairs decreases with increasing n_d^{th} and totally disappears when every fourth site is driven in a chain of fixed length N [as shown in Figs. 13(d) and 13(h)]. This follows from the consistent behavior of \mathcal{R} [as shown in Figs. 13(e)–13(h)] which was conjectured in the main text as a requirement for the emergence of SZM. We note here that the lower value of $|\langle \Phi_r^- | S_1^x | \Phi_r^+ \rangle|$ for $s_d = \{1\}$ compared to the value for other higher n_d^{th} is not an artifact of just the presence of ghost pairs. There are many pairs with $|\langle \Phi_r^- | S_1^x | \Phi_r^+ \rangle|$ a bit less than 0.5 for direct pairing albeit much higher than the corresponding value for cross pairing. Such pairs also reduce in number and disappear with increasing n_d^{th} , ramping up the value of $|\langle \Phi_r^- | S_1^x | \Phi_r^+ \rangle|$ towards 0.5. The parallel approach of all the \mathcal{R}_r towards one enable us to arrive at the condition: $S_1^x | \Phi_r^\pm \rangle = \frac{1}{2} e^{\pm i\theta_r} | \Phi_r^\mp \rangle$ via the ansatz used in Eq. (22) in the main text.

In Fig. 14, we show the behavior of S_1^{vN} for all the Floquet eigenstates in parallel with the behaviors of $\delta_r^\pm = \langle \xi_r^\pm | \xi_r^\pm \rangle$. There are lots of low-entangled Floquet eigenstates for $s_d = \{1\}$ but all of them get strongly entangled for $s_d = \{1, 5\}$. This is accompanied by a huge reduction in the average value of $|\delta^\pm|$, we denote by $|\delta^\pm|$. Further increase of driven sites (n_d^{th})

is found to reduce $|\delta^\pm|$ only a little bit. Consequently, the entanglement spectrum also becomes only slightly narrower, though by now they are already saturated at their maximal value to a good extent. Thus in the asymptotic limit, when every fourth site is driven, the boundary spin forms Bell like pairing with the rest of the system in all the Floquet eigenstates.

APPENDIX F: SEMIANALYTICAL STUDY OF THE PAIRING-GAP

We now seek to have some more understanding of the vanishing of the pairing gap which is given by

$$\begin{aligned} \Delta_r &= \langle \Phi_r^+ | H_F | \Phi_r^+ \rangle - \langle \Phi_r^- | H_F | \Phi_r^- \rangle \\ &= \frac{1}{2} [(\langle \rightarrow, \xi_r^+ | H_F | \rightarrow, \xi_r^+ \rangle - \langle \rightarrow, \xi_r^- | H_F | \rightarrow, \xi_r^- \rangle) \\ &\quad + (\langle \leftarrow, \bar{\xi}_r^+ | H_F | \leftarrow, \bar{\xi}_r^+ \rangle - \langle \leftarrow, \bar{\xi}_r^- | H_F | \leftarrow, \bar{\xi}_r^- \rangle)] \\ &\quad + \text{Re}[\langle \rightarrow, \xi_r^+ | H_F | \leftarrow, \bar{\xi}_r^+ \rangle] + \text{Re}[\langle \rightarrow, \xi_r^- | H_F | \leftarrow, \bar{\xi}_r^- \rangle], \end{aligned} \tag{F1}$$

The quantities inside the first parenthesis in the second and third line of Eq. (F1) get canceled with the emergence of SZM due to the condition $\mathcal{R}_r \approx 1$, which we have verified numerically. The vanishing of the quantities in the last line of Eq. (F1) (let us call it Δ_r') is less straightforward to see and here we will adapt a semi-analytical approach to understand

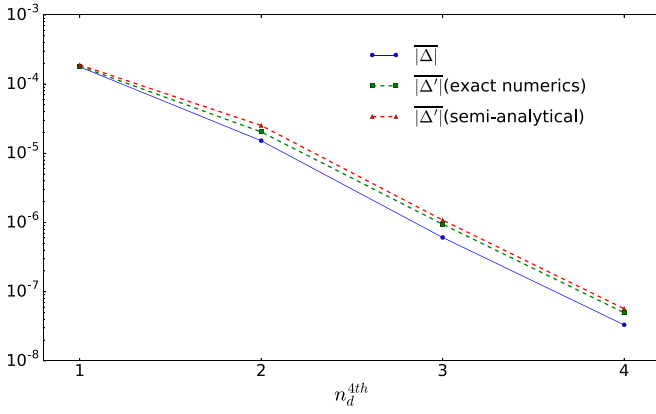


FIG. 15. Comparison of the scaling of $|\overline{\Delta}|$ and $|\overline{\Delta}'|$. The latter is calculated from exact numerics as well as using a semianalytical expression [Eq. (F3)]. Parameters: $h = 1$, $\gamma = 15$, $\omega = \omega_m^1 = 7.53$, and $N = 14$.

this. To this end, we first decompose H_F into three parts: $H_F = h_A^F + h_{A,B}^F + h_B^F$, where the subscripts denote part of the chain (sites) on which each term is supported: A and B represent site 1 and rest of the chain respectively, whereas $h_{A,B}^F$ represent terms that connect these two parts,

$$\begin{aligned}
 h_{A,B}^F = & -S_1^x S_2^x \\
 & - \left[\left(\frac{\sin \lambda}{\lambda} - a_4(\mathbf{p}) \right) S_1^y S_2^y + \left(\frac{\sin \lambda}{\lambda} - a_3(\mathbf{p}) \right) S_1^z S_2^z \right] \\
 & + \left[\left(\frac{1 - \cos \lambda}{\lambda} + a_5(\mathbf{p}) \right) S_1^z S_2^y \right. \\
 & \left. - \left(\frac{1 - \cos \lambda}{\lambda} - a_6(\mathbf{p}) \right) S_1^y S_2^z \right] + H_{F,\text{nonloc}}^{(2)}. \quad (\text{F2})
 \end{aligned}$$

The purpose of such decomposition of the Floquet Hamiltonian together with the eigenstates as in Eq. (22) will be clear now. We first note that $\langle \rightarrow | h_A^F | \leftarrow \rangle$ is nothing but $H_F(2, 1)$ as discussed in Sec. III. Secondly, note that though we have quite accurate knowledge of h_A^F and $h_{A,B}^F$, the analytical structure of h_B^F is not very well known particularly for multisite driving. The former also remain almost unchanged as we increase $n_d^{4\text{th}}$ but the latter must change drastically with it. However, $\langle \rightarrow, \xi_r^\pm | h_B^F | \leftarrow, \bar{\xi}_r^\pm \rangle = 0$ and hence h_B^F has zero contribution in Δ'_r . This enables us to write down a semianalytical expression of Δ'_r ,

$$\begin{aligned}
 \Delta'_r = & \text{Re} \left[\langle \rightarrow | h_A^F | \leftarrow \rangle (\delta_r^+ + \delta_r^-) + \langle \rightarrow, \xi_r^+ | h_{A,B}^F | \leftarrow, \bar{\xi}_r^+ \rangle \right. \\
 & \left. + \langle \rightarrow, \xi_r^- | h_{A,B}^F | \leftarrow, \bar{\xi}_r^- \rangle \right]. \quad (\text{F3})
 \end{aligned}$$

$\langle \rightarrow | h_A^F | \leftarrow \rangle$ becomes very small at $\omega \approx \omega_m$ whereas $|\delta^\pm|$ get smaller with increasing $n_d^{4\text{th}}$. We found in Appendix E that $|\overline{\delta^\pm}|$ reduces strongly when we go from $n_d^{4\text{th}} = 1$ ($s_d = \{1\}$) to $n_d^{4\text{th}} = 2$ ($s_d = \{1, 5\}$) but further increase in $n_d^{4\text{th}}$ does not reduce the value of $|\overline{\delta^\pm}|$ much (Fig. 14). Interestingly, the contribution to the gap (Δ) which comes only from the real part of these complex numbers, gets significantly smaller due to some cancellations between δ^\pm . We compare $|\overline{\Delta}'|$ from Eq. (F3) with fully exact numerics [using the final line of Eq. (F1)] in Fig. 15 and find very good agreement. Moreover, we find, $|\overline{\Delta}'|$ itself is not much different than $|\overline{\Delta}|$. This again implies that our understanding of the structure of the Floquet Hamiltonian is quite accurate.

-
- [1] B. M. Terhal, Quantum error correction for quantum memories, *Rev. Mod. Phys.* **87**, 307 (2015).
- [2] C. Nayak, S. H. Simon, A. Stern, M. Freedman, and S. D. Sarma, Non-Abelian anyons and topological quantum computation, *Rev. Mod. Phys.* **80**, 1083 (2008).
- [3] S. D. Sarma, M. Freedman, and C. Nayak, Majorana zero modes and topological quantum computation, *npj Quantum Inf.* **1**, 15001 (2015).
- [4] J. Majer, J. M. Chow, J. M. Gambetta, J. Koch, B. R. Johnson, J. A. Schreier, L. Frunzio, D. I. Schuster, A. A. Houck, A. Wallraff *et al.*, Coupling superconducting qubits via a cavity bus, *Nature (London)* **449**, 443 (2007).
- [5] S. M. Girvin, Circuit QED: superconducting qubits coupled to microwave photons, in *Quantum Machines: Measurement and Control of Engineered Quantum Systems: Lecture Notes of the Les Houches Summer School: Volume 96, July 2011* (Oxford University Press, Oxford, 2014), pp. 113–256.
- [6] L.-M. Duan and C. Monroe, Colloquium: Quantum networks with trapped ions, *Rev. Mod. Phys.* **82**, 1209 (2010).
- [7] D. H. Dunlap and V. M. Kenkre, Dynamic localization of a charged particle moving under the influence of an electric field, *Phys. Rev. B* **34**, 3625 (1986).
- [8] A. Eckardt, M. Holthaus, H. Lignier, A. Zenesini, D. Ciampini, O. Morsch, and E. Arimondo, Exploring dynamic localization with a Bose-Einstein condensate, *Phys. Rev. A* **79**, 013611 (2009).
- [9] T. Oka and H. Aoki, Photovoltaic Hall effect in graphene, *Phys. Rev. B* **79**, 081406(R) (2009).
- [10] T. Kitagawa, T. Oka, A. Brataas, L. Fu, and E. Demler, Transport properties of nonequilibrium systems under the application of light: Photoinduced quantum Hall insulators without Landau levels, *Phys. Rev. B* **84**, 235108 (2011).
- [11] M. S. Rudner, N. H. Lindner, E. Berg, and M. Levin, Anomalous edge states and the bulk-edge correspondence for periodically driven two-dimensional systems, *Phys. Rev. X* **3**, 031005 (2013).
- [12] Y. H. Wang, H. Steinberg, P. Jarillo-Herrero, and N. Gedik, Observation of Floquet-Bloch states on the surface of a topological insulator, *Science* **342**, 453 (2013).
- [13] G. Jotzu, M. Messer, R. Desbuquois, M. Lebrat, T. Uehlinger, D. Greif, and T. Esslinger, Experimental realization of the topological Haldane model with ultracold fermions, *Nature (London)* **515**, 237 (2014).

- [14] K. Sacha and J. Zakrzewski, Time crystals: a review, *Rep. Prog. Phys.* **81**, 016401 (2018).
- [15] D. V. Else, C. Monroe, C. Nayak, and N. Y. Yao, Discrete time crystals, *Annu. Rev. Condens. Matter Phys.* **11**, 467 (2020).
- [16] V. Khemani, R. Moessner, and S. L. Sondhi, A brief history of time crystals, [arXiv:1910.10745](https://arxiv.org/abs/1910.10745).
- [17] D. V. Else, B. Bauer, and C. Nayak, Prethermal phases of matter protected by time-translation symmetry, *Phys. Rev. X* **7**, 011026 (2017).
- [18] D. Bluvstein, A. Omran, H. Levine, A. Keesling, G. Semeghini, S. Ebadi, T. T. Wang, A. A. Michailidis, N. Maskara, W. W. Ho, S. Choi, M. Serbyn, M. Greiner, V. Vuletić, and M. D. Lukin, Controlling quantum many-body dynamics in driven Rydberg atom arrays, *Science* **371**, 1355 (2021).
- [19] N. Maskara, A. A. Michailidis, W. W. Ho, D. Bluvstein, S. Choi, M. D. Lukin, and M. Serbyn, Discrete time-crystalline order enabled by quantum many-body scars: Entanglement steering via periodic driving, *Phys. Rev. Lett.* **127**, 090602 (2021).
- [20] J. O'Sullivan, O. Lunt, C. W. Zollitsch, M. Thewalt, J. J. Morton, and A. Pal, Signatures of discrete time crystalline order in dissipative spin ensembles, *New J. Phys.* **22**, 085001 (2020).
- [21] J. Randall, C. Bradley, F. van der Gronden, A. Galicia, M. Abobeih, M. Markham, D. Twitchen, F. Machado, N. Yao, and T. Taminiua, Many-body-localized discrete time crystal with a programmable spin-based quantum simulator, *Science* **374**, 1474 (2021).
- [22] M. Sato, S. Takayoshi, and T. Oka, Laser-driven multiferroics and ultrafast spin current generation, *Phys. Rev. Lett.* **117**, 147202 (2016).
- [23] R. Moessner and S. L. Sondhi, Equilibration and order in quantum Floquet matter, *Nat. Phys.* **13**, 424 (2017).
- [24] T. Oka and S. Kitamura, Floquet engineering of quantum materials, *Annu. Rev. Condens. Matter Phys.* **10**, 387 (2019).
- [25] M. S. Rudner and N. H. Lindner, Band structure engineering and non-equilibrium dynamics in Floquet topological insulators, *Nat. Rev. Phys.* **2**, 229 (2020).
- [26] K. Wintersperger, C. Braun, F. N. Únal, A. Eckardt, M. D. Liberto, N. Goldman, I. Bloch, and M. Aidelsburger, Realization of an anomalous Floquet topological system with ultracold atoms, *Nat. Phys.* **16**, 1058 (2020).
- [27] L. D'Alessio and M. Rigol, Long-time behavior of isolated periodically driven interacting lattice systems, *Phys. Rev. X* **4**, 041048 (2014).
- [28] A. Lazarides, A. Das, and R. Moessner, Equilibrium states of generic quantum systems subject to periodic driving, *Phys. Rev. E* **90**, 012110 (2014).
- [29] C. J. Turner, A. A. Michailidis, D. A. Abanin, M. Serbyn, and Z. Papić, Weak ergodicity breaking from quantum many-body scars, *Nat. Phys.* **14**, 745 (2018).
- [30] M. Serbyn, D. A. Abanin, and Z. Papić, Quantum many-body scars and weak breaking of ergodicity, *Nat. Phys.* **17**, 675 (2021).
- [31] S. Moudgalya, N. Regnault, and B. A. Bernevig, Entanglement of exact excited states of affleck-kennedy-lieb-tasaki models: Exact results, many-body scars, and violation of the strong eigenstate thermalization hypothesis, *Phys. Rev. B* **98**, 235156 (2018).
- [32] S. Moudgalya, S. Rachel, B. A. Bernevig, and N. Regnault, Exact excited states of nonintegrable models, *Phys. Rev. B* **98**, 235155 (2018).
- [33] S. Moudgalya, B. A. Bernevig, and N. Regnault, Quantum many-body scars and Hilbert space fragmentation: a review of exact results, *Rep. Prog. Phys.* **85**, 086501 (2022).
- [34] K. Lee, R. Melendrez, A. Pal, and H. J. Changlani, Exact three-colored quantum scars from geometric frustration, *Phys. Rev. B* **101**, 241111 (2020).
- [35] K. Pakrouski, P. N. Pallegar, F. K. Popov, and I. R. Klebanov, Many-body scars as a group invariant sector of Hilbert space, *Phys. Rev. Lett.* **125**, 230602 (2020).
- [36] J. Jeyaretnam, J. Richter, and A. Pal, Quantum scars and bulk coherence in a symmetry-protected topological phase, *Phys. Rev. B* **104**, 014424 (2021).
- [37] K. Sanada, Y. Miao, and H. Katsura, Quantum many-body scars in spin models with multi-body interactions, *Phys. Rev. B* **108**, 155102 (2023).
- [38] P. Sala, T. Rakovszky, R. Verresen, M. Knap, and F. Pollmann, Ergodicity breaking arising from hilbert space fragmentation in dipole-conserving hamiltonians, *Phys. Rev. X* **10**, 011047 (2020).
- [39] V. Khemani, M. Hermele, and R. Nandkishore, Localization from hilbert space shattering: From theory to physical realizations, *Phys. Rev. B* **101**, 174204 (2020).
- [40] K. Lee, A. Pal, and H. J. Changlani, Frustration-induced emergent Hilbert space fragmentation, *Phys. Rev. B* **103**, 235133 (2021).
- [41] S. Moudgalya and O. I. Motrunich, Hilbert space fragmentation and commutant algebras, *Phys. Rev. X* **12**, 011050 (2022).
- [42] B. Mukherjee, D. Banerjee, K. Sengupta, and A. Sen, Minimal model for hilbert space fragmentation with local constraints, *Phys. Rev. B* **104**, 155117 (2021).
- [43] J. Richter and A. Pal, Anomalous hydrodynamics in a class of scarred frustration-free hamiltonians, *Phys. Rev. Res.* **4**, L012003 (2022).
- [44] A. Smith, J. Knolle, D. L. Kovrizhin, and R. Moessner, Disorder-free localization, *Phys. Rev. Lett.* **118**, 266601 (2017).
- [45] N. Chakraborty, M. Heyl, P. Karpov, and R. Moessner, Disorder-free localization transition in a two-dimensional lattice gauge theory, *Phys. Rev. B* **106**, L060308 (2022).
- [46] P. Fendley, Strong zero modes and eigenstate phase transitions in the XYZ/interacting Majorana chain, *J. Phys. A: Math. Theor.* **49**, 30LT01 (2016).
- [47] J. Kemp, N. Y. Yao, C. R. Laumann, and P. Fendley, Long coherence times for edge spins, *J. Stat. Mech.: Theory Exp.* (2017) 063105.
- [48] D. V. Else, P. Fendley, J. Kemp, and C. Nayak, Prethermal strong zero modes and topological qubits, *Phys. Rev. X* **7**, 041062 (2017).
- [49] D. J. Yates, A. G. Abanov, and A. Mitra, Lifetime of almost strong edge-mode operators in one-dimensional, interacting, symmetry protected topological phases, *Phys. Rev. Lett.* **124**, 206803 (2020).
- [50] D. J. Yates, A. G. Abanov, and A. Mitra, Dynamics of almost strong edge modes in spin chains away from integrability, *Phys. Rev. B* **102**, 195419 (2020).

- [51] T. Rakovszky, P. Sala, R. Verresen, M. Knap, and F. Pollmann, Statistical localization: From strong fragmentation to strong edge modes, *Phys. Rev. B* **101**, 125126 (2020).
- [52] D. J. Yates, F. H. L. Essler, and A. Mitra, Almost strong $(0, \pi)$ edge modes in clean interacting one-dimensional floquet systems, *Phys. Rev. B* **99**, 205419 (2019).
- [53] D. J. Yates and A. Mitra, Strong and almost strong modes of floquet spin chains in Krylov subspaces, *Phys. Rev. B* **104**, 195121 (2021).
- [54] D. Abanin, W. De Roeck, W. W. Ho, and F. H. L. Essler, A rigorous theory of many-body prethermalization for periodically driven and closed quantum systems, *Commun. Math. Phys.* **354**, 809 (2017).
- [55] D. A. Abanin, W. De Roeck, and F. H. L. Essler, Exponentially slow heating in periodically driven many-body systems, *Phys. Rev. Lett.* **115**, 256803 (2015).
- [56] T. Kuwahara, T. Mori, and K. Saito, Floquet-magnus theory and generic transient dynamics in periodically driven many-body quantum systems, *Ann. Phys.* **367**, 96 (2016).
- [57] A. Rubio-Abadal, M. Ippoliti, S. Hollerith, D. Wei, J. Rui, S. L. Sondhi, V. Khemani, C. Gross, and I. Bloch, Floquet prethermalization in a bose-hubbard system, *Phys. Rev. X* **10**, 021044 (2020).
- [58] K. Agarwal and I. Martin, Dynamical enhancement of symmetries in many-body systems, *Phys. Rev. Lett.* **125**, 080602 (2020).
- [59] M. Bukov, L. D'Alessio, and A. Polkovnikov, Universal high-frequency behavior of periodically driven systems: from dynamical stabilization to floquet engineering, *Adv. Phys.* **64**, 139 (2015).
- [60] T. Mikami, S. Kitamura, K. Yasuda, N. Tsuji, T. Oka, and H. Aoki, Brillouin-wigner theory for high-frequency expansion in periodically driven systems: Application to floquet topological insulators, *Phys. Rev. B* **93**, 144307 (2016).
- [61] A. Eckardt and E. Anisimovas, High-frequency approximation for periodically driven quantum systems from a floquet-space perspective, *New J. Phys.* **17**, 093039 (2015).
- [62] B. Mukherjee, S. Nandy, A. Sen, D. Sen, and K. Sengupta, Collapse and revival of quantum many-body scars via floquet engineering, *Phys. Rev. B* **101**, 245107 (2020).
- [63] S. Pai and M. Pretko, Dynamical scar states in driven fracton systems, *Phys. Rev. Lett.* **123**, 136401 (2019).
- [64] B. Mukherjee, A. Sen, D. Sen, and K. Sengupta, Dynamics of the vacuum state in a periodically driven rydberg chain, *Phys. Rev. B* **102**, 075123 (2020).
- [65] A. Hudomal, J.-Y. Desautels, B. Mukherjee, G.-X. Su, J. C. Halimeh, and Z. Papić, Driving quantum many-body scars in the PXP model, *Phys. Rev. B* **106**, 104302 (2022).
- [66] A. A. Michailidis, C. J. Turner, Z. Papić, D. A. Abanin, and M. Serbyn, Stabilizing two-dimensional quantum scars by deformation and synchronization, *Phys. Rev. Res.* **2**, 022065(R) (2020).
- [67] P.-G. Rozon, M. J. Gullans, and K. Agarwal, Constructing quantum many-body scar hamiltonians from floquet automata, *Phys. Rev. B* **106**, 184304 (2022).
- [68] A. Das, Exotic freezing of response in a quantum many-body system, *Phys. Rev. B* **82**, 172402 (2010).
- [69] A. Haldar, D. Sen, R. Moessner, and A. Das, Dynamical freezing and scar points in strongly driven floquet matter: Resonance vs emergent conservation laws, *Phys. Rev. X* **11**, 021008 (2021).
- [70] S. Kar, B. Mukherjee, and K. Sengupta, Tuning towards dynamic freezing using a two-rate protocol, *Phys. Rev. B* **94**, 075130 (2016).
- [71] R. Melendrez, B. Mukherjee, P. Sharma, A. Pal, and H. J. Changlani, Real space thermalization of locally driven quantum magnets, [arXiv:2212.13790](https://arxiv.org/abs/2212.13790) (2022).
- [72] X. Wen, R. Fan, and A. Vishwanath, Floquet's refrigerator: Conformal cooling in driven quantum critical systems, [arXiv:2211.00040](https://arxiv.org/abs/2211.00040) (2022).
- [73] K. Hida, Crossover between the haldane-gap phase and the dimer phase in the spin-1/2 alternating heisenberg chain, *Phys. Rev. B* **45**, 2207 (1992).
- [74] T. Kennedy and H. Tasaki, Hidden $z_2 \times z_2$ symmetry breaking in haldane-gap antiferromagnets, *Phys. Rev. B* **45**, 304 (1992).
- [75] K. Hida, Ground-state phase diagram of the spin-1/2 ferromagnetic-antiferromagnetic alternating heisenberg chain with anisotropy, *Phys. Rev. B* **46**, 8268 (1992).
- [76] H. Manaka, I. Yamada, and K. Yamaguchi, Ferromagnetic-dominant alternating heisenberg chains with ferromagnetic and antiferromagnetic interactions formed in $(\text{CH}_3)_2\text{CHNH}_3\text{CuCl}_3$, *J. Phys. Soc. Jpn.* **66**, 564 (1997).
- [77] H. Manaka and I. Yamada, Formation of alternating antiferromagnetic Heisenberg chains in $(\text{CH}_3)_2\text{CHNH}_3\text{CuBr}_3$, *J. Phys. Soc. Jpn.* **66**, 1908 (1997).
- [78] C. J. Turner, A. A. Michailidis, D. A. Abanin, M. Serbyn, and Z. Papić, Quantum scarred eigenstates in a Rydberg atom chain: Entanglement, breakdown of thermalization, and stability to perturbations, *Phys. Rev. B* **98**, 155134 (2018).
- [79] M. Schechter and T. Iadecola, Many-body spectral reflection symmetry and protected infinite-temperature degeneracy, *Phys. Rev. B* **98**, 035139 (2018).
- [80] D. Banerjee and A. Sen, Quantum scars from zero modes in an Abelian lattice Gauge theory on ladders, *Phys. Rev. Lett.* **126**, 220601 (2021).
- [81] B. Mukherjee, Z. Cai, and W. V. Liu, Constraint-induced breaking and restoration of ergodicity in spin-1 PXP models, *Phys. Rev. Res.* **3**, 033201 (2021).
- [82] P. Sharma, K. Lee, and H. J. Changlani, Multimagnon dynamics and thermalization in the $s = 1$ easy-axis ferromagnetic chain, *Phys. Rev. B* **105**, 054413 (2022).
- [83] G. Benenti, G. Casati, T. Prosen, D. Rossini, and M. Žnidarič, Charge and spin transport in strongly correlated one-dimensional quantum systems driven far from equilibrium, *Phys. Rev. B* **80**, 035110 (2009).
- [84] F. Haake, *Quantum Signatures of Chaos*, 3rd ed., Springer Series in Synergetics (Springer, Berlin, Germany, 2010).
- [85] J. Kemp, N. Y. Yao, and C. R. Laumann, Symmetry-enhanced boundary qubits at infinite temperature, *Phys. Rev. Lett.* **125**, 200506 (2020).
- [86] D. Thuberg, S. A. Reyes, and S. Eggert, Quantum resonance catastrophe for conductance through a periodically driven barrier, *Phys. Rev. B* **93**, 180301(R) (2016).
- [87] A. Agarwala and D. Sen, Effects of local periodic driving on transport and generation of bound states, *Phys. Rev. B* **96**, 104309 (2017).
- [88] F. Hübner, C. Daur, S. Eggert, C. Kollath, and A. Sheikhan, Floquet-engineered pair and single-particle filters in the fermi-hubbard model, *Phys. Rev. A* **106**, 043303 (2022).

- [89] H. Bernien, S. Schwartz, A. Keesling, H. Levine, A. Omran, H. Pichler, S. Choi, A. S. Zibrov, M. Endres, M. Greiner, V. Vuletic, and M. D. Lukin, Probing many-body dynamics on a 51-atom quantum simulator, *Nature (London)* **551**, 579 (2017).
- [90] W. L. Tan, P. Becker, F. Liu, G. Pagano, K. S. Collins, A. De, L. Feng, H. B. Kaplan, A. Kyprianidis, R. Lundgren *et al.*, Domain-wall confinement and dynamics in a quantum simulator, *Nat. Phys.* **17**, 742 (2021).
- [91] P. N. Jepsen, Y. K. E. Lee, H. Lin, I. Dimitrova, Y. Margalit, W. W. Ho, and W. Ketterle, Long-lived phantom helix states in Heisenberg quantum magnets, *Nat. Phys.* **18**, 899 (2022).
- [92] R. Islam, R. Ma, P. M. Preiss, M. Eric Tai, A. Lukin, M. Rispoli, and M. Greiner, Measuring entanglement entropy in a quantum many-body system, *Nature (London)* **528**, 77 (2015).
- [93] T. Brydges, A. Elben, P. Jurcevic, B. Vermersch, C. Maier, B. P. Lanyon, P. Zoller, R. Blatt, and C. F. Roos, Probing rényi entanglement entropy via randomized measurements, *Science* **364**, 260 (2019).
- [94] D. Bluvstein, H. Levine, G. Semeghini, T. T. Wang, S. Ebadi, M. Kalinowski *et al.*, A quantum processor based on coherent transport of entangled atom arrays, *Nature (London)* **604**, 451 (2022).
- [95] N. O’Dea, F. Burnell, A. Chandran, and V. Khemani, From tunnels to towers: Quantum scars from lie algebras and q -deformed lie algebras, *Phys. Rev. Res.* **2**, 043305 (2020).
- [96] G. Vidal, Efficient simulation of one-dimensional quantum many-body systems, *Phys. Rev. Lett.* **93**, 040502 (2004).
- [97] S. R. White and A. E. Feiguin, Real-time evolution using the density matrix renormalization group, *Phys. Rev. Lett.* **93**, 076401 (2004).
- [98] M. Fishman, S. R. White, and E. M. Stoudenmire, The ITensor software library for tensor network calculations, *SciPost Phys. Codebases*, 4 (2022).
- [99] S. Vajna, K. Klobas, T. Prosen, and A. Polkovnikov, Replica resummation of the Baker-Campbell-Hausdorff series, *Phys. Rev. Lett.* **120**, 200607 (2018).
- [100] L. D’Alessio and A. Polkovnikov, Many-body energy localization transition in periodically driven systems, *Ann. Phys.* **333**, 19 (2013).
- [101] J. M. Deutsch, Quantum statistical mechanics in a closed system, *Phys. Rev. A* **43**, 2046 (1991).
- [102] M. Srednicki, Chaos and quantum thermalization, *Phys. Rev. E* **50**, 888 (1994).
- [103] M. Rigol, V. Dunjko, and M. Olshanii, Thermalization and its mechanism for generic isolated quantum systems, *Nature (London)* **452**, 854 (2008).
- [104] G. Ramírez, J. Rodríguez-Laguna, and G. Sierra, Entanglement over the rainbow, *J. Stat. Mech.: Theory Exp.* (2015) P06002.
- [105] C. M. Langlett, Z.-C. Yang, J. Wildeboer, A. V. Gorshkov, T. Iadecola, and S. Xu, Rainbow scars: From area to volume law, *Phys. Rev. B* **105**, L060301 (2022).
- [106] A. Verdeny, A. Mielke, and F. Mintert, Accurate effective hamiltonians via unitary flow in floquet space, *Phys. Rev. Lett.* **111**, 175301 (2013).
- [107] A. Chandran, A. Pal, C. R. Laumann, and A. Scardicchio, Many-body localization beyond eigenstates in all dimensions, *Phys. Rev. B* **94**, 144203 (2016).
- [108] A. K. Kulshreshtha, A. Pal, T. B. Wahl, and S. H. Simon, Behavior of l-bits near the many-body localization transition, *Phys. Rev. B* **98**, 184201 (2018).
- [109] T. M. Graham, Y. Song, J. Scott, C. Poole, L. Phuttitarn, K. Jooya, P. Eichler, X. Jiang *et al.*, Multi-qubit entanglement and algorithms on a neutral-atom quantum computer, *Nature (London)* **604**, 457 (2022).
- [110] D. Bluvstein, S. J. Evered, A. A. Geim, S. H. Li, H. Zhou, T. Manovitz, S. Ebadi, M. Cain, M. Kalinowski, D. Hangleiter, J. P. B. Ataides, N. Maskara, I. Cong, X. Gao, P. S. Rodriguez, T. Karolyshyn, G. Semeghini, M. J. Gullans, M. Greiner, V. Vuletić *et al.*, Logical quantum processor based on reconfigurable atom arrays, *Nature (London)* **626**, 58 (2024).
- [111] L. S. Martin, H. Zhou, N. T. Leitao, N. Maskara, O. Makarova, H. Gao, Q.-Z. Zhu, M. Park, M. Tyler, H. Park, S. Choi, and M. D. Lukin, Controlling local thermalization dynamics in a floquet-engineered dipolar ensemble, *Phys. Rev. Lett.* **130**, 210403 (2023).
- [112] S. Nadj-Perge, I. K. Drozdov, J. Li, H. Chen, S. Jeon, J. Seo, A. H. MacDonald, B. A. Bernevig, and A. Yazdani, Observation of Majorana fermions in ferromagnetic atomic chains on a superconductor, *Science* **346**, 602 (2014).
- [113] R. M. Lutchyn, E. P. A. M. Bakkers, L. P. Kouwenhoven, P. Krogstrup, C. M. Marcus, and Y. Oreg, Majorana zero modes in superconductor–semiconductor heterostructures, *Nat. Rev. Mater.* **3**, 52 (2018).
- [114] T. Martin, I. Martin, and K. Agarwal, Effect of quasiperiodic and random noise on many-body dynamical decoupling protocols, *Phys. Rev. B* **106**, 134306 (2022).
- [115] A. Morvan, T. Andersen, X. Mi, C. Neill, A. Petukhov, K. Kechedzhi, D. Abanin, A. Michailidis, R. Acharya, F. Arute *et al.*, Formation of robust bound states of interacting microwave photons, *Nature (London)* **612**, 240 (2022).
- [116] T. Prosen, Driven quantum bits push computational limit, *Nature (London)* **612**, 217 (2022).
- [117] B. Mukherjee, M. Szyniszewski, A. Pal, H. J. Changlani, and R. Melendrez, Research data for the paper “Emergent strong zero mode through local Floquet engineering” (2024), doi: 10.5522/04/25061525.
- [118] M. P. Grabowski and P. Mathieu, Integrability test for spin chains, *J. Phys. A: Math. Gen.* **28**, 4777 (1995).